REVIEW

In Situ TEM Experiments of Electrochemical Lithiation and Delithiation of Individual Nanostructures

Xiao Hua Liu, Yang Liu, Akihiro Kushima, Sulin Zhang, Ting Zhu,* Ju Li,* and Jian Yu Huang*

Understanding the microscopic mechanisms of electrochemical reaction and material degradation is crucial for the rational design of high-performance lithium ion batteries (LIBs). A novel nanobattery assembly and testing platform inside a transmission electron microscope (TEM) has been designed, which allows a direct study of the structural evolution of individual nanowire or nanoparticle electrodes with near-atomic resolution in real time. In this review, recent progresses in the study of several important anode materials are summarized. The consistency between in situ and ex situ results is shown, thereby validating the new in situ testing paradigm. Comparisons between a variety of nanostructures lead to the conclusion that electrochemical reaction and mechanical degradation are material specific, size dependent, and geometrically and compositionally sensitive. For example, a highly anisotropic lithiation in Si is observed, in contrast to the nearly isotropic response in Ge. The Ge nanowires can develop a spongy network, a unique mechanism for mitigating the large volume changes during cycling. The Si nanoparticles show a critical size of ~150 nm below which fracture is averted during lithiation, and above which surface cracking, rather than central cracking, is observed. In carbonaceous nanomaterials, the lithiated multi-walled carbon nanotubes (MWCNTs) are drastically embrittled, while few-layer graphene nanoribbons remain mechanically robust after lithiation. This distinct contrast manifests a strong 'geometrical embrittlement' effect as compared to a relatively weak 'chemical embrittlement' effect. In oxide nanowires, discrete cracks in ZnO nanowires are generated near the lithiation reaction front, leading to leapfrog cracking, while a mobile dislocation cloud at the reaction front is observed in SnO_2 nanowires. This contrast is corroborated by ab initio calculations that indicate a strong chemical embrittlement of ZnO, but not of SnO_2, after a small amount of lithium insertion. In metallic nanowires such as Al, delithiation causes pulverization, and the product nanoparticles are held in place by the surface Li-Al-O glass tube, suggesting possible strategies for improving electrode cyclability by coatings. In addition, a new in situ chemical lithiation method is introduced for fast screening of battery materials by conventional TEM. Evidently, in situ nanobattery experiments inside TEM are a powerful approach for advancing the fundamental understanding of electrochemical reactions and materials degradation and therefore pave the way toward rational design of high-performance LIBs.

1. Introduction

Lithium ion batteries (LIBs) have received significant attention as they are being considered for the power supply of electric vehicles and the power backup of intermittent energy systems, etc.[1–3] To meet the ever-increasing requirements for such demanding applications, new materials and chemistries must be developed to achieve high energy density, high power capability, and long lifetime.[3–5] Radical progress, although highly desired, has not been achieved so far,[6] owing to the intrinsic complexity of LIBs, i.e., many electrochemical, physical, and mechanical processes are concurrently taking place during their operation. To improve the overall performance, a LIB must be designed such that all these concerted processes are operated in a predictable manner across multiple interfaces. Currently, many aspects of the fundamental science with respect to battery operation remain poorly understood, such as the atomic mechanisms of lithiation-delithiation, electrode degradation, electrolyte decomposition, evolution of solid electrolyte interphase (SEI), and the size effects on the transport kinetics, mechanics, and degradation of nanomaterial-based electrodes, to name a few.

Carbonaceous anodes are widely used in current LIBs. But the theoretical capacity is only 372 mAh/g for graphite. Potential replacements, such as Si and Ge, have a much higher energy density than graphite, but they suffer from severe degradation due to the large volume changes during the electrochemical cycling (i.e., lithiation

Dr. X. H. Liu, Dr. Y. Liu, Dr. J. Y. Huang
Center for Integrated Nanotechnologies (CINT)
Sandia National Laboratories
Albuquerque, New Mexico 87185, USA
E-mail: jhuang@sandia.gov
Prof. S. Zhang
Department of Engineering Science and Mechanics
Pennsylvania State University
University Park, Pennsylvania 16802, USA

Prof. T. Zhu
Woodruff School of Mechanical Engineering
Georgia Institute of Technology
Atlanta, Georgia 30332, USA
E-mail: ting.zhu@me.gatech.edu
Dr. A. Kushima, Prof. J. Li
Department of Nuclear Science and Engineering and Department of Materials Science and Engineering
Massachusetts Institute of Technology
Cambridge, Massachusetts 02139, USA
E-mail: liju@mit.edu; Website: http://li.mit.edu

Materials
Views
www.MaterialsViews.com

ADVANCED
ENERGY
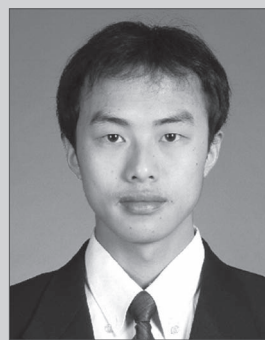MATERIALS
www.advenergymat.de

REVIEW

and delithiation). Nanostructured and nanocomposite materials are being widely explored for the next-generation LIBs. Compared to their bulk counterparts, the larger surface-to-volume ratio of nanomaterials can enable fast charge/mass transport and facile strain relaxation,[7,8] thereby offering a pathway for nanoengineered LIBs with enhanced performance.

To shed light on the fundamental science and to improve battery design, it is important to probe the reaction kinetics and microstructural evolution during battery operation. There have been growing interests in developing various in situ techniques for battery studies, such as optical microscopy,[9,10] scanning electron microscopy (SEM),[11,12] transmission electron microscopy (TEM),[13–15] X-ray diffraction (XRD),[16–18] nuclear magnetic resonance (NMR) spectroscopy,[19–21] transmission X-ray microscopy (TXM),[22] and Raman spectroscopy.[23,24] These in situ studies have provided important insights into the phase transformation and material degradation mechanisms. For instance, the equilibrium Li-Si binary phase diagram indicates four distinct Li-Si phases ($Li_{12}Si_7$, Li_7Si_3, $Li_{13}Si_4$, and $Li_{22}Si_5$),[25] and spontaneous electrochemical alloying (SEA) was believed to be an effective way to screen the alloy phases at ambient temperature;[26] for Li-Si system, the $Li_{22}Si_5$ phase has long been considered as the fully lithiated phase for a Si anode at room temperature.[27–29] However, by monitoring the changes of crystal structure during lithiation of crystalline Si (c-Si) with in situ XRD, Obrovac et al. discovered a new crystalline $Li_{15}Si_4$ (c-$Li_{15}Si_4$) phase,[16] which does not appear in the equilibrium Li-Si binary phase diagram.[27] The $Li_{15}Si_4$ phase as the fully lithiated product for Si anodes at room temperature was later verified by many investigations, using techniques such as in situ TEM,[30,31] in situ NMR,[20,21] and in situ XRD.[17,18] This example shows that the electrochemical reactions could be considerably far from reversible equilibrium processes. It also demonstrates the importance of in situ studies. A brief review on the in situ techniques for LIB studies was available in an earlier review article.[15]

Among the many in situ techniques, in situ TEM offers a unique capability of resolving the microstructural evolution of the electrode materials at high tempo-spatial resolutions.[13,32,33] The main challenge of in situ TEM electrochemistry is that the volatile organic electrolytes are incompatible with the high-vacuum environment required for TEM observations.[15] To circumvent this difficulty, we demonstrated the "open-cell" concept by creating the first working nanobattery in the TEM (**Figure 1**a) using an individual SnO_2 nanowire anode, an ionic liquid electrolyte (ILE), and a bulk $LiCoO_2$ cathode, and observed the microstructural evolution during the electrochemical lithiation.[13] This liquid-cell technique was later adapted to a half cell using a solid-state lithium oxide (Li_2O) electrolyte and a Li metal as the counter electrode.[30] This development enables the in situ observation of extremely small objects such as a single nanoparticle with sizes down to a few nanometers.[15] Using this all-solid nanobattery technique we have studied several anode materials of both fundamental and technical importance, such as Si,[30,31,34,35] Ge,[36] Al,[37] multi-walled carbon nanotubes (MWCNTs),[38] graphene,[39] and ZnO[40] as well as a few cathode materials such as $LiFePO_4$.

Figure 1 shows a schematic illustration of the in situ TEM nanobattery setup.[13,15,30,31,34–36,38–42] For studying anode materials, the key components of the nanobattery include an

Xiao Hua Liu received his BS from Department of Materials Science and Engineering in Tsinghua University in 2003, and his PhD from Beijing National Center for Electron Microscopy (BNCEM) in Tsinghua University in 2008. His research interests include nanoscale materials for renewable energy, energy storage, and in situ transmission electron microscopy.

Ju Li is Battelle Energy Alliance Professor of Nuclear Science and Engineering and a full professor of Materials Science and Engineering at MIT. Using atomistic modeling and in situ experimental observations, his group investigate mechanical, electrochemical and transport behaviors of materials, often under extreme stress, temperature and radiation environments, as well as novel means of energy storage and conversion. Ju was a winner of 2005 Presidential Early Career Award for Scientists and Engineers, the 2006 MRS Outstanding Young Investigator Award, and 2007 TR35 award from *Technology Review* magazine.

Jian Yu Huang is currently a principle member of technical staff at the Center for Integrated Nanotechnologies (CINT), Sandia National Laboratories in Albuquerque. He received his BS from Xiangtan University in 1990 and PhD from Institute of Metal Research, Chinese Academy of Sciences in 1996. His primary research interests are centered on in situ electron microscopy of nanostructured materials. He intends to bridge the gap between microstructure characterizations and property measurements by conducting integrated studies on the microstructure and electrical, mechanical, thermal, optical and electrochemical properties of individual nanostructures, such as carbon nanotubes, nanowires, and nanoparticles.

electron transparent anode (such as nanowires, nanoparticles, and thin foils), a vacuum-compatible electrolyte (such as ionic liquids, polymer or other inorganic solid-state electrolytes), and a bulk Li source (such as a discharged cathode). Depending on

REVIEW
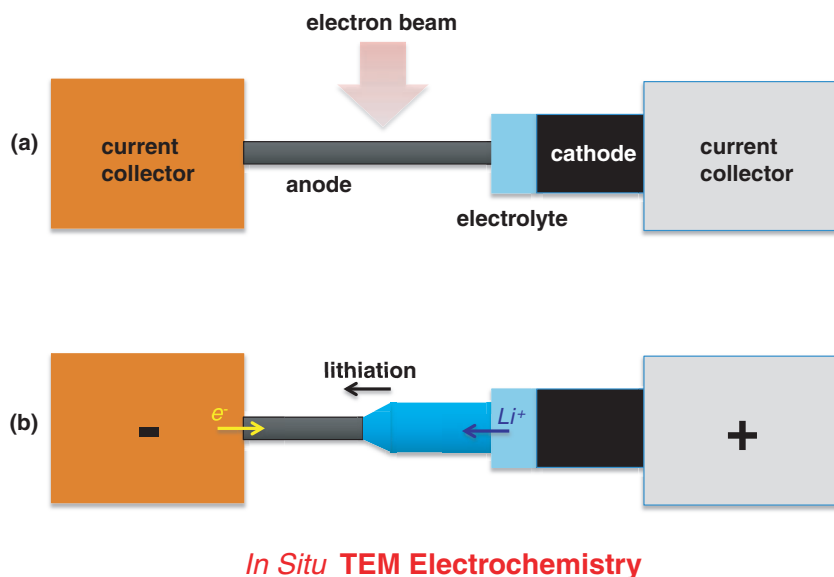
In Situ **TEM Electrochemistry**

Figure 1. Schematic illustration of in situ TEM electrochemical tests setup. (a) A nanobattery setup for anode study. The key components include an electron-transparent anode (such as a nanowire or nanoparticle), a vacuum-compatible electrolyte (such as ionic liquid, polymer or solid-state electrolyte), a stable Li source (such as a bulk discharged cathode) and the current collectors. (b) Operation of the nanobattery for lithiation of the anode. Potential is applied to the current collectors to drive the electrons and Li ions flow across the circuit, and the micro-structural evolution is monitored in real time. The setup may be adapted for studies such as the cathode or other interfaces in the nanobattery.

the focus of the study, any electron-transparent electrode or interface could be investigated by this technique.

There are several major differences in the experimental setup between the in situ TEM electrochemistry and a conventional ex situ electrochemical cell or a real battery: (1) Cell geometry: only one end of the single nanowire, nanotube, or nanoparticle electrode is brought to contact with the electrolyte in the former,[13] while electrodes are immersed in an electrolyte in the latter (so-called "flooding geometry"[6,42]). Recently we have demonstrated that flooding experiments can also be realized with an in situ TEM setup.[42] (2) Electrolyte: vacuum-compatible electrolyte must be used in the former,[6,13] such as room-temperature ionic liquid electrolyte (LiTFSI/P_{14}TFSI; LiTFSI denoting lithium bis (trifluoromethylsulfonyl) imide; P_{14}TFSI denoting 1-butyl-1-methylpyrrolidinium bis (trifluoromethylsulfonyl) imide). The ionic conductivity in ionic liquid electrolyte is significantly lower than that in the conventional organic EC/DMC (EC denoting ethylene carbonate; DMC denoting dimethyl carbonate) electrolyte.[32] Another example is Li_2O. It is an electron-insulating but ion-conducting material at the nanoscale,[13,30] and is not usually considered as an electrolyte in conventional cells. (3) Beam effect: any material subjected to the in situ TEM study will unavoidably be exposed to the high energy (80 ~ 300 keV) electron beam in contrast to the "dark" environment in real batteries, which may modify the material properties or electrochemical reactions.[15] Therefore, in our in situ TEM experiments, the control experiments are always conducted to verify observations in the illuminated experiments. This review will also make comparisons between in situ TEM and more conventional ex situ electrochemical studies to validate the former.
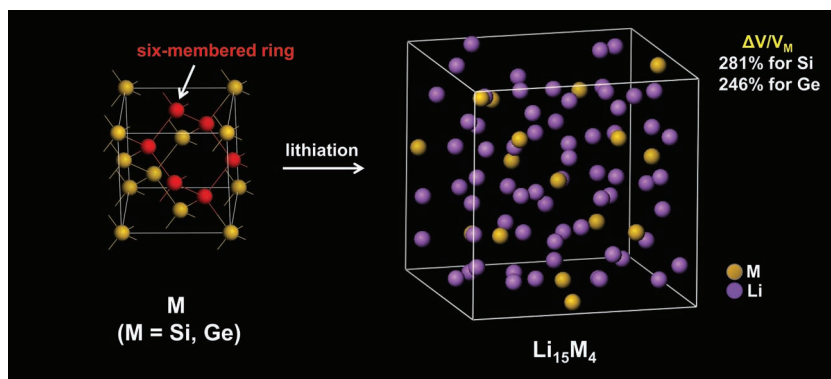
Here we summarize the recent progress in the studies of anode materials with the in situ TEM electrochemistry technique. This review emphasizes "comparison" and "verification", i.e., by comparing (1) the electrochemical behavior of structurally similar materials or polymorphs; and (2) the results obtained from the in situ nanobattery experiments and those from ex situ electrochemical tests in conventional macroscopic cells. The review is divided into the following sections. In Section 2, the cycling behavior of two important anode materials with the same diamond cubic crystal structure, i.e. Si and Ge, will be compared. In Section 3, the post-lithiation properties of carbonaceous materials, MWCNTs versus few-layer graphene nanoribbons (GNRs) will be compared to illustrate a lithium embrittlement effect. In Section 4, different mechano-electrochemical effects of brittle oxides (ZnO, SnO_2) will be compared, to illustrate a lithium embrittlement effect of a chemical origin, which is different from the carbonaceous materials. In Section 5, pulverization of the Al nanowires as well as the evolution of the thin alumina (Al_2O_3) surface layer during cycling is shown. Finally, in Section 6, a new in situ technique based on conventional TEM instrument, i.e., without specially designed TEM holders, will be presented. Such development allows for a wider application of the in situ TEM technique as a quick screening tool for the battery materials. Based on the comparison of the in situ and ex situ experiments, we conclude that the in situ nanobattery TEM experiment is a novel technique for gaining fundamental understanding of the operative mechanisms in real LIBs, despite the apparently different experimental conditions between the in situ and ex situ cells.

2. Si versus Ge

Some of the Group IV materials, including Si, Ge, Sn and their compounds, have received considerable attention as candidates for LIB anodes, because they have much higher lithium storage densities than the carbonaceous anodes used in current LIBs.[43] Si is of particular interest for its high theoretical capacity, 4200 mAh/g for $Li_{22}Si_5$ at high temperature[25,44] or 3579 mAh/g for $Li_{15}Si_4$ at room temperature.[16,45] There have been a large number of ongoing studies of the Si anode materials in different forms, such as single crystals,[46] polycrystalline thin films,[27] amorphous films,[47,48] nanoparticles,[49] nanowires,[7,50,51] nanotubes,[52] composites with conductive materials (carbon,[31,49,53–58] nickel,[7,16] etc.) and doped Si.[23,31,59,60]

Compared to Si, the iso-structural Ge has gained much less attention,[61–71] despite having a comparable volumetric capacity (7366 Ah/L for $Li_{15}Ge_4$ versus 8334 Ah/L for $Li_{15}Si_4$).[36,43,62] Ge has a lower gravimetric capacity of 1384 mAh/g for $Li_{15}Ge_4$ (about 40% of that of Si) than Si, but it is still much higher than those of graphite and Sn. Moreover, Ge has a smaller band-gap ($E_g = 0.6$ eV) than Si ($E_g = 1.1$ eV), and thus a higher intrinsic

Materials Views
www.MaterialsViews.com

**ADVANCED
ENERGY
MATERIALS**
www.advenergymat.de

REVIEW

Figure 2. Phase transformation of Si and Ge anodes from pristine to fully lithiated states. At room temperature, Si and Ge expand by 281% and 246% if lithiated to the $Li_{15}M_4$ phase (M = Si, Ge). The basic structural unit is a six-membered ring (highlighted with red balls) enclosed by strong covalent bonds in pristine Si and Ge, which collapses into isolated atoms in the fully lithiated $Li_{15}M_4$ phases.

electronic conductivity, which is desirable for high power capability. The high rate capability of thin film Ge electrodes has been demonstrated up to 1000 °C.[72] Compared to Si, a practical disadvantage of Ge is its high cost. In our in situ experiments, Ge electrodes in the forms of nanowires,[36] nanoparticles, and thin films, indeed showed superior properties in terms of high rate capability, cyclability, and stability. The detailed comparison of the electrochemical cycling results between Si and Ge are discussed in the following.

2.1. Phase Transformation during Electrochemical Cycling

As promising anode materials in the same column of the Periodic Table, Si and Ge have many similarities. First of all, Si and Ge both undergo significant structural changes during cycling. **Figure 2** shows the huge volumetric expansion upon the first lithiation, 281% for Si and 246% for Ge through alloying with Li to form the crystalline $Li_{15}M_4$ (M = Si or Ge) phases, which is much larger than the volume change of graphite (<10%) through a Li-intercalation mechanism. Both the pristine Si and Ge crystals have the diamond cubic crystal structure, in which the atoms are tetrahedrally bonded and the characteristic structural unit is the six-membered ring (highlighted by the red balls in Figure 2). During lithiation, the Si-Si bonds are broken to form five-membered rings, "Y"-shaped Si-Si_3 stars, dimers, and finally isolated Si in $Li_{15}Si_4$.[20,21,73] The Si-Si distances are greater than 4.5 Å in the $Li_{15}Si_4$ lattice,[20] as compared to the 2.35 Å bonds in the six-membered ring of pristine Si. One of the major and common problems with the Si and

Ge anodes is the large volume changes during cycling. This could cause fracture, loss of electrical contact, and pulverization of electrodes, manifested as rapid capacity fading.[43,74]

Si and Ge exhibit similar cyclic voltammograms (CVs),[45,62,68] suggesting the qualitatively similar electrochemical processes and phase transformations upon Li insertion and extraction. During lithiation, crystalline Si and Ge adopt a two-step reaction process to reach the fully lithiated $Li_{15}M_4$ phases.[31,36,45,62,68] Namely, the crystals are first converted to the amorphous alloys of Li_xM (a-Li_xM, $0 < x < 3.75$) through electrochemically-driven solid-state amorphization (ESA), which is then followed by crystallization of a-Li_xM to c-$Li_{15}M_4$. **Figure 3**a shows a typical CV for Si,[75] in which the two broad lithiation peaks marked as "A" and "B"
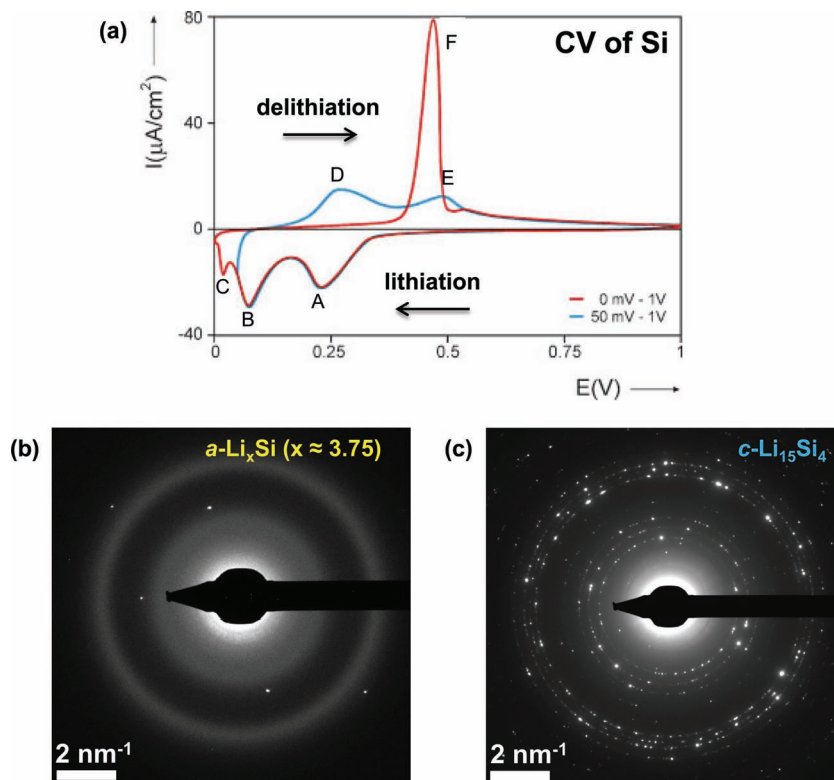
Figure 3. Typical phase transformation routes of Si during electrochemical cycling. (a) Cyclic voltammogram (CV) of Si. Depending on the cutoff potential used during lithiation, the CV curve show different peaks, i.e., only two broad peaks (marked as "A" and "B" in the blue curve) appear if the cutoff is 50 mV or above versus Li^+/Li, and the third sharp peak (marked as "C" in the red curve) appears if the cutoff is 0 mV, corresponding to the crystallization process of the amorphous Li-Si (a-Li_xSi, x ~ 3.75) alloy to the crystalline $Li_{15}Si_4$ (c-$Li_{15}Si_4$) phase. Accordingly, the delithiation process from a-Li_xSi shows two broad peaks (marked as "D" and "E") but a sharp peak (marked as "F") from c-$Li_{15}Si_4$. (b,c) Typical electron diffraction patterns (EDP) from a-Li_xSi and c-$Li_{15}Si_4$ observed in the in situ lithiation experiments of Si. The similarity of intensity distribution of the EDPs between the amorphous (Figure 3b) and the crystalline (Figure 3c) phases implies that the a-Li_xSi phase is structurally close to the c-$Li_{15}Si_4$ phase. The structures of Li-Si alloy phases corresponding to Peaks "A", "B", "D", "E", and "F" (Figure 3a) are not clear. Reproduced with permission.[75]

correspond to the ESA process, and the sharp tiny peak marked as "C" corresponds to the sudden crystallization of a-Li$_x$Si ($x \approx 3.75$) to c-Li$_{15}$Si$_4$. Figures 3b and c show the electron diffraction patterns (EDPs) from the a-Li$_x$Si ($x \approx 3.75$) and c-Li$_{15}$Si$_4$ phases obtained in the in situ lithiation experiments,[31] respectively, which are consistent with the ex situ electrochemical results.[16–18,45] The final lithiated phase appears to be dependent on the cutoff potential during lithiation,[62,68,75] which may suppress formation of the c-Li$_{15}$M$_4$ phases (e.g., using 50 mV cutoff for the blue curve in Figure 3a). Interestingly, the delithiation peaks are highly dependent on the lithiated states, showing two broad peaks (marked as "D" and "E" in Figure 3a) from a-Li$_x$M (M = Si or Ge, $x \approx 3.75$) or a single sharp peak (marked as "F") from c-Li$_{15}$M$_4$, respectively. The same dependence of the delithiation peaks on the lithiated states has been observed for both Si and Ge,[16,45,62,68,75] but the reason is not well understood. It was recently found that doping conditions could also influence the positions of the peaks.[23] Overall, the phase transformations in the electrochemical lithiation and delithiation processes are similar between Si and Ge. With increasing Li content, the difference between Li$_x$Si and Li$_x$Ge becomes progressively small. For instance, the diamond cubic Si and Ge ($x = 0$) show a 4.2% difference in their lattice parameters, but the difference is only 0.9% between the Li$_{15}$Si$_4$ and Li$_{15}$Ge$_4$ phases (i.e., $x = 3.75$).

Formation of similar Li$_{15}$Si$_4$ and Li$_{15}$Ge$_4$ phases was observed in conventional electrochemical cells.[16,18,45,61,62,65,76] The consistency of the observed Li$_{15}$M$_4$ phases between the in situ[15,30,31,36] and the ex situ electrochemical experiments[16,18,62,68,76] demonstrates that in situ TEM electrochemical experiments can capture the main feature of the electrochemical processes occurring in conventional electrochemical cells. Furthermore, opportunities are opened up for in situ TEM studies to identify the unknown Li-Si or Li-Ge phases corresponding to other peaks in the CV (Figure 3a, except for the known Li$_{15}$M$_4$ phase for Peak "C").[27] It is worth noting that the phase formation sequence in the electrochemical process is likely to differ from that in equilibrium phase diagram. For instance, the established Li$_{15}$M$_4$ phase observed in many independent experiments was not included in the phase diagram of the equilibrium phases.[25,27,29,77] With the high spatial resolution and analytical capability of TEM, it is possible to incorporate the controlled electrochemical characterization methods into the in situ TEM experiments,[15] such as galvanostatic charging and cyclic voltammetry, so as to screen all the intermetallic phases in the CVs of Si and Ge. Such development will be highly promising for advancing the fundamental understanding of the lithiation and delithiation mechanisms.

2.2. Mechano-Electrochemical Effects

Although the electrochemical reaction products are similar between Si and Ge, their lithiation kinetics and associated mechanical

responses are markedly different. First, the volume expansion of c-Si during the first lithiation is highly anisotropic,[30,46,78] with the predominant expansion along the <110> directions and little expansion along the <111> directions. In contrast, the volume expansion of c-Ge during the first lithiation is largely isotropic.[36] Second, due to the different band structures and electronic properties, Si lithiation is sensitive to the change of doping condition and electrical conductivity,[23,31] but Ge is not because of its high intrinsic conductivity.[65]

2.2.1. Anisotropic Lithiation of Si

Several recent studies have clearly shown that the lithiation of Si is highly dependent on the crystallographic orientations,[30,46,78] resembling the anisotropic etching of Si.[79,80] **Figure 4** shows the microstructural evolution of a Si nanowire with a <112> growth direction during the in situ lithiation process. Once the Si nanowire contacted the Li$_2$O/Li electrode and a negative potential of -2 V was applied to the nanowire, lithiation proceeded both axially and radially. The c-Si nanowire was converted to a-Li$_x$Si alloy, which was further crystallized to the c-Li$_{15}$Si$_4$ phase after full lithiation. The interface between the c-Si and the Li-Si alloy was atomically sharp (Figure 4a). The lithiated part showed a unique contrast with two parallel subwires separated by a central white line (Figure 4a,b). Close-up view at the lithiated nanowire revealed a central crack running along the nanowire axis (Figure 4c). It has been determined that a lithiated <112> Si nanowire exhibits a unique dumbbell-shaped cross section,[30] as illustrated in Figure 4d, showing the largest swelling along the radial <110> directions and the smallest swelling along the radial <111> directions.
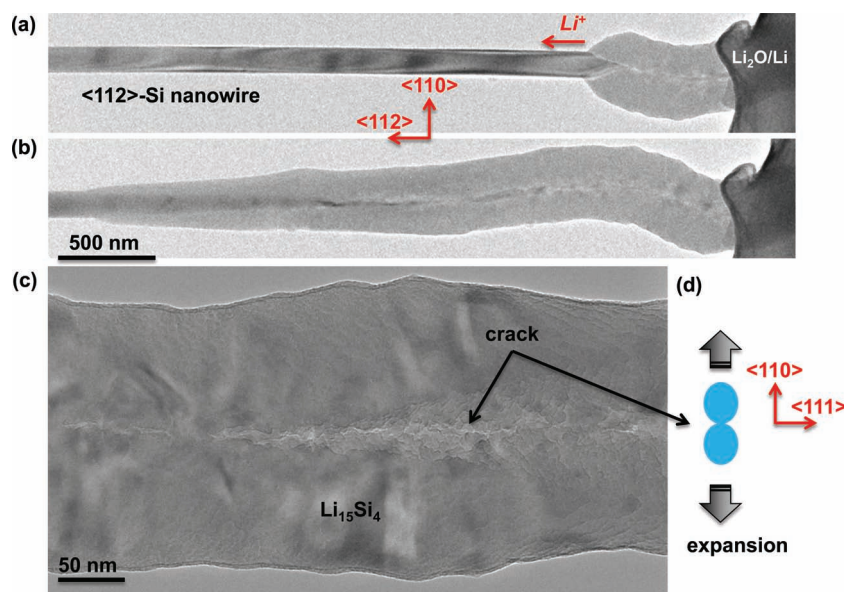
Figure 4. Anisotropic swelling and cracking of a <112>-Si nanowire. (a,b) Snapshots showing progressive lithiation along both the axial and radial directions. The radial swelling was anisotropic, as evidenced by the white contrast in the center of the lithiated nanowire. (c) Enlarged image showing the central crack in the lithiated Si nanowire. (d) Schematic illustration of the dumbbell-shaped cross section of a lithiated <112>-Si nanowire viewed along the <112> axial direction. A central crack developed due to hoop stress and much larger swelling along the <110> directions than that along the <111> directions.

www.MaterialsViews.com

ADVANCED
ENERGY
MATERIALS
www.advenergymat.de

REVIEW
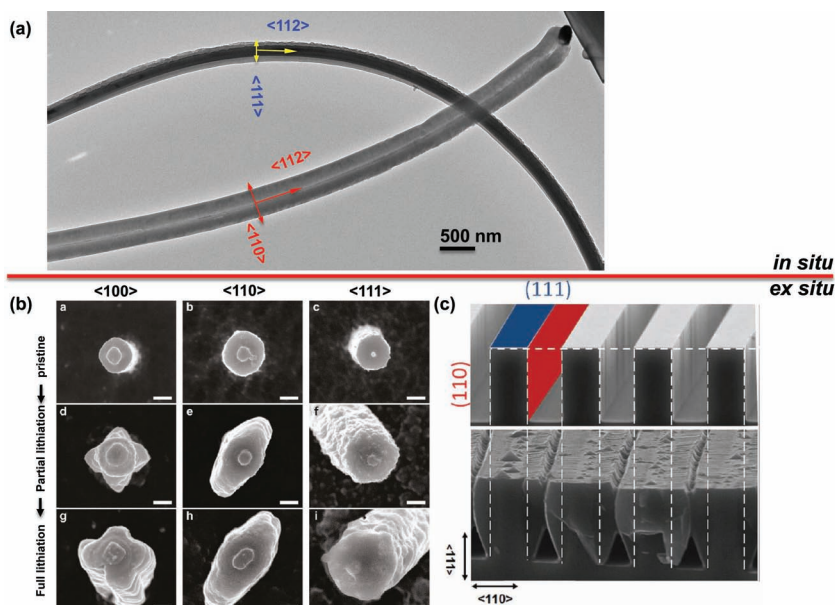
Figure 5. Comparison of in situ and ex situ results on the anisotropic lithiation of crystalline Si. (a) <112>-Si nanowires with large swelling along <110> but much less swelling along <111> revealed in the in situ TEM experiments. (b) Anisotropic radial lithiation of Si pillars with different orientations in conventional ex situ cells. Preferential lithiation along <110> directions leads to formation of different cross sections with shapes of 4-fold, 2-fold, and 6-fold symmetries for <100>, <110>, and <111> pillars, respectively. (c) Dominant swelling along <110> in Si slabs but little swelling along <111>. All these in situ and ex situ studies reveal that lithiation occurs along the <110> directions of crystalline Si. Reproduced with permission.[46,78] Copyright 2011, American Chemical Society and Wiley.

nanopillars (Figure 5b), respectively. Similarly, in an independent study by Goldman et al., predominant swelling along the <110> directions was observed in Si microslabs in the ex situ experiments (Figure 5c).[46] These mutually consistent results suggest that the anisotropy of Si lithiation is an intrinsic property of Li-Si alloying reaction, largely independent of the experimental conditions. On the other hand, the lithiation process can be regarded as analogous to the etching process of c-Si, and the anisotropy in lithiation is similar to the established anisotropic etching of c-Si,[79,80] which has been widely exploited in the microelectronics industry.

2.2.2. Isotropic Lithiation of Ge

Interestingly, despite the same diamond cubic crystal structure and same growth direction along <112> as Si, Ge nanowires showed markedly different mechanical responses in the in situ lithiation experiments.[36] **Figure 6** shows the typical microstructural change of a <112>-Ge nanowire in the first lithiation process. The pristine Ge nanowire was straight (Figure 6a). Upon Li insertion, it swelled along both axial and radial directions, resulting in an elongated and thickened wire (Figure 6b) with uniform amorphous contrast (Figure 6d). This morphology suggests an isotropic swelling along all directions during lithiation. The EDPs before and after lithiation confirm the phase transformation from single crystalline Ge (c-Ge, Figure 6e) to a Li-rich amorphous phase of Li-Ge (a-Li_xGe, $\times \sim 3.75$, Figure 6f), which eventually crystallizes to the c-$Li_{15}Ge_4$ phase.[36] The EDP from this a-Li_xGe (x ~ 3.75) phase is characterized by two broad
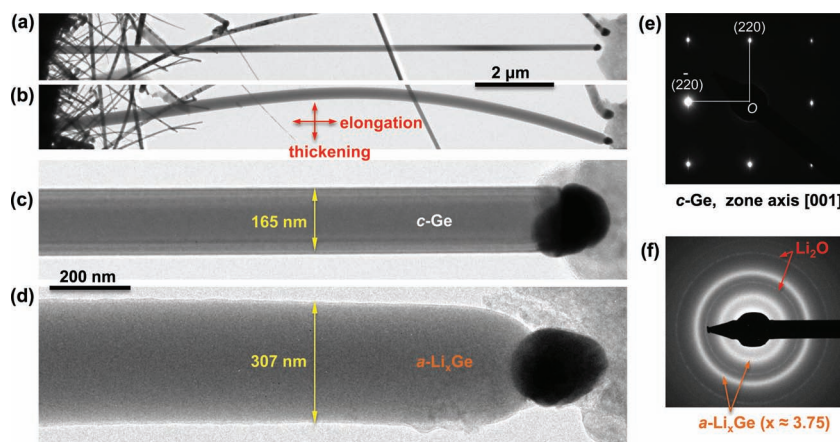
The anisotropic swelling creates a thinned center along the nanowire axis, leading to the formation of the apparent longitudinal crack along the wire that causes self-splitting of the single nanowire into two subwires.[30]

The anisotropic lithiation is intrinsic to the Li-Si alloying process, regardless of the experimental procedures, as evidenced by the consistent observations in both the in situ (**Figure 5**a) and ex situ experiments (Figure 5b-c), which were performed under different experimental conditions and with different cell geometries.[30,46,78] For the <112> Si nanowires, there are orthogonal <110> and <111> radial directions in the cross section, which happen to exhibit the largest anisotropy with the fastest lithiation occurring in the former direction and the slowest lithiation occurring in the latter direction, respectively.[30] Indeed, the diameter increases by over 200% along <110>, but less than 10% along <111> (Figure 5a). Lee et al. fabricated Si pillars with different orientations and conducted electrochemical lithiation in a conventional cell.[78] They observed anomalous shape change of the cross sections in those Si pillars, which was highly dependent on the crystallographic directions, as manifested by the 4-fold, 2-fold and 6-fold swelling in <100>, <110> and <111> oriented

Figure 6. Isotropic swelling of a <112>-Ge nanowire without cracking during lithiation. (a) A pristine Ge nanowire. (b) The lithiated nanowire with obvious elongation. (c-d) Close-up images showing tip region of the nanowire before (c) and after lithiation (d). There was no central crack as seen in the <112>-Si nanowire in Figure 4. (e-f) EDPs showing the phase transformation from the initial single crystalline Ge (c-Ge) to amorphous Li-Ge (a-Li_xGe) alloy after lithiation.

REVIEW
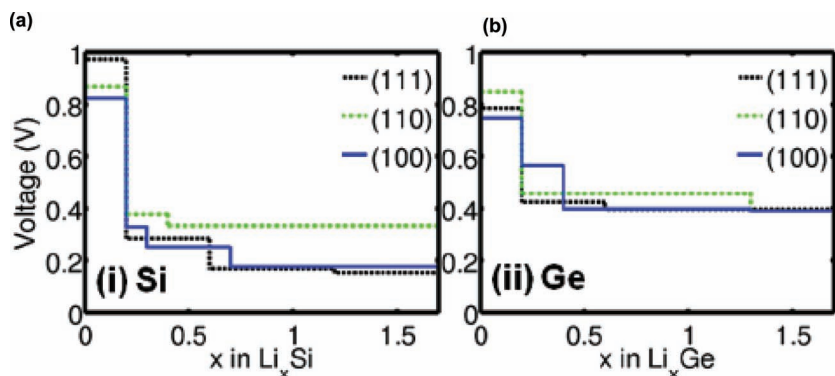
Figure 7. Comparison of voltage profiles for different crystallographic planes of Si and Ge. (a) The onset voltage for lithiation of Si (110) plane is higher than that of (111) and (100) planes, consistent with the experimentally observed preferential lithiation along Si <110>. (b) In contrast to Si, Ge (111), (110), and (100) planes show similar onset lithiation voltages, consistent with the experimental observation of isotropic lithiation in *c*-Ge. The initial stages with the voltage over 0.6 V or the Li-to-Si ratio x < 0.2 are not related to the alloying process but the surface states. Reproduced with permission.[65] Copyright 2011, American Chemical Society.

halos, with intensity distribution similar to that from a crystallized $Li_{15}Ge_4$ pattern.[81,82] The anisotropic swelling and central cracking seen in the <112>-Si nanowires (Figure 4) were not observed during lithiation of the Ge nanowires.

The amorphous products of lithiated Si and Ge are both isotropic in nature based on the EDPs. Several questions then arise: What is the origin of the lithiation anisotropy in Si? Why does not such anisotropy appear in Ge? Since Li diffusivity tensor in the diamond cubic lattice of Si and Ge is known to be isotropic in the dilute limit, the lithiation anisotropy must be related to different properties of the crystallographic planes of unlithiated Si crystals that adjoin the amorphous product. In other words, the orientation dependence of interfacial mobility (or equivalently reaction rate) at the sharp boundary of two phases (i.e., pristine crystal and amorphous phase of lithiated product) is expected to govern the lithiation anisotropy in Si, rather than long-range transport.[83] Chan et al. studied the lithiation onset voltage of (100), (110) and (111) Si and Ge single crystals with in situ Raman spectroscopy and density function theory (DFT) calculations. **Figure 7** shows that the calculated onset lithiation potential of Si (110) plane is higher than that of the (111) and (100) planes (except for the initial surface reactions corresponding to regions with the voltage over 0.6 V or the Li-to-Si ratio, x, less than ∼ 0.2), but there is no obvious lithiation potential difference between the different planes in Ge.[65] This is consistent with the experimental observations showing that Si has high anisotropy with the fastest lithiation on (110) planes, in contrast to Ge that undergoes nearly isotropic lithiation.[30,36]

The anisotropic lithiation and swelling of *c*-Si must be taken into consideration in the electrode design, by either taking advantage of or suppressing it via electrode geometry

design. It is also suggested that "isotropic" materials, such as Ge and amorphous Si,[36,84] may be a better choice for stable electrodes. In the following section, we show that Ge nanowire anodes possess another remarkable property of nanopore formation during delithiation, which enhances the mechanical stability of the electrode during cycling.[36]
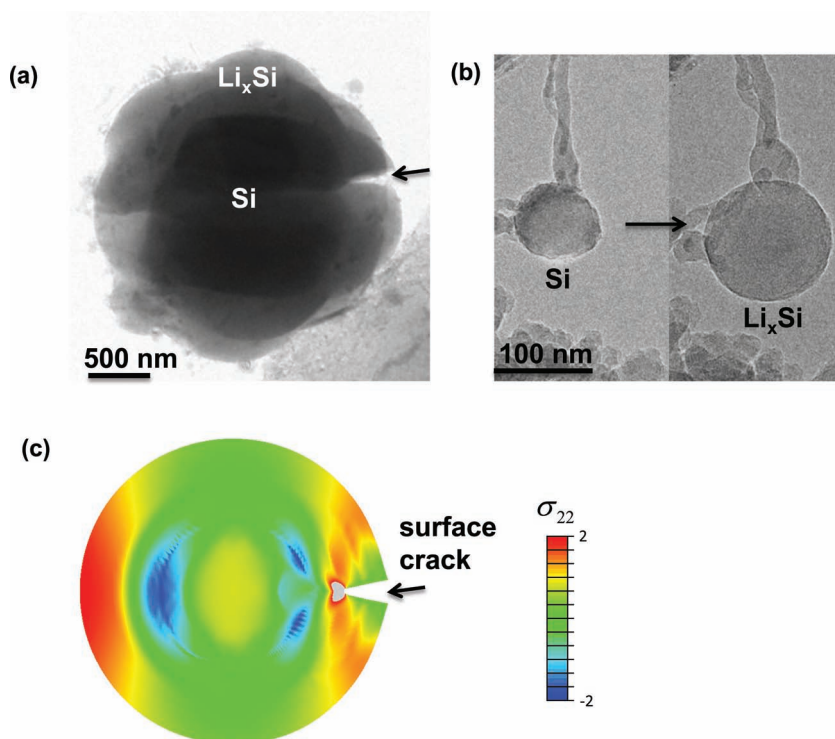
2.3. Nanopore Formation in Ge Nanowires during Delithiation

It has been shown that Ge nanowires undergo nearly isotropic lithiation without fracture. From an electrochemical cycling viewpoint, it is equally important to know whether or not they form cracks during delithiation. **Figure 8** shows that instead of cracking, the lithiated Ge nanowires exhibited porous structures after Li was extracted in either a liquid cell (Figure 8a) or a solid cell (Figure 8b) during the in situ TEM experiments. Such porous Ge structure was also found in an ex situ cell after cycling (Figure 8c),[69] indicating again the high consistency between the in situ and ex situ studies, although the experimental conditions between the two techniques differ considerably. The formation of such spongy structure involves aggregation of vacancies produced by Li extraction, similar to the formation of porous metals by selective dealloying. More importantly, the three dimensional (3D) network of the amorphous Ge ligands is quite stable during cycling, as evidenced by the similar pore distribution and morphology after each delithiation process (so-called "pore memory effect").[36]

Both the in situ and ex situ electrochemical tests indicate that Ge is a good anode material and has the following merits: (1) high capacity, with volumetric capacity comparable to Si and much higher gravimetric capacity than graphite;[36] (2) high rate capability, up to 1000C for a 250-nm thick Ge film,[72] as compared to only 30C demonstrated in a 50-nm thick *a*-Si film;[84] (3) high mechanical stability, without fracture or cracking during both lithiation and delithiation.[36]
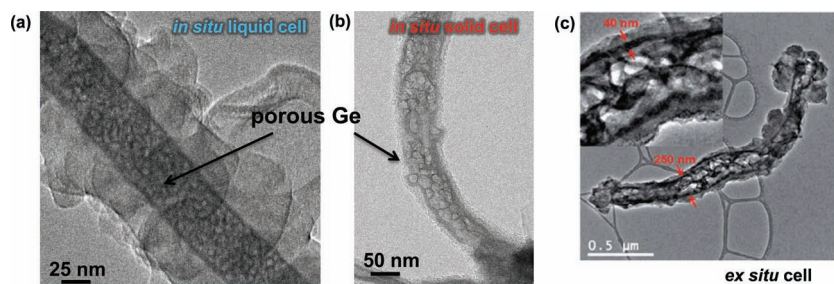
Figure 8. Nanopore formation in Ge observed in both in situ and ex situ cycling experiments. (a,b) Porous Ge nanowires after delithiation in a liquid cell using the ionic liquid electrolyte (a), or in a solid cell using Li_2O solid electrolyte (b). (c) Porous Ge obtained after cycling in a conventional half cell. Reproduced with permission.[36,69] Copyright 2011, American Chemical Society and Wiley.

Materials
Views
www.MaterialsViews.com

ADVANCED
ENERGY
MATERIALS
www.advenergymat.de

REVIEW

Figure 9. Size dependent fracture and surface cracking in Si nanoparticles during lithiation. (a) In situ experimental observation showing a crack nucleates from the surface of the a-Li$_x$Si shell and propagates inwards during lithiation of a large Si nanoparticle with diameter of 1800 nm. (b) Lithiation of a small Si nanoparticle without cracking. The diameter increased from 80 nm to 130 nm. (c) Simulation showing that the surface cracking occurs due to the large tensile hoop stress induced by lithiation-induced volumetric expansion. Reproduced with permission.[34] Copyright 2012, American Chemical Society.

2.4. Size-Dependent Fracture of Si Nanoparticles during Lithiation

Nanoengineering is one of the most promising strategies to mitigate the fracture of high-capacity anodes.[74] It has been reported that Si nanoparticles and nanowires show better cyclability than their bulk counterparts.[7,8,49] One of the fundamental questions is: under what critical size fracture can be prevented during lithiation. We studied the lithiation of individual Si nanoparticles with different sizes in the range of a few tens of nanometers to several micrometers, and revealed a strong size dependence of fracture during the first lithiation process.[15,34] For large Si nanoparticles with diameters above ~150 nm, cracks always nucleated from the surface (**Figure 9**a), and the nanoparticle fractured into pieces upon further lithiation.[15] On the contrary, small Si nanoparticles did not crack, but exhibited a huge volume expansion upon completion of lithiation, resembling an inflated balloon (Figure 9b).[15,34] This in situ result clearly demonstrates that nanostructures are indeed better in terms of averting the adverse mechanical consequence accompanying the electrochemical reactions. If the small Si nanoparticles are dispersed in a flexible elastomeric or porous matrix, the huge volume changes may be well accommodated.

An unexpected observation from the in situ lithiation experiments is that cracking in large Si nanoparticles always

initiates from the surface of a lithiated shell of a-Li$_x$Si, not from the center of c-Si core (Figure 9a and 9c). This surface-cracking mode is different from the prediction by previous models on the first nucleation of a central crack.[85–87] To understand the surface cracking and the size-dependent fracture in Si nanoparticles, the following physical effects must be taken into account: (1) two-phase lithiation mechanism;[34,88] and (2) the curvature of the two-phase boundary. These two effects combine to cause the reversal of hoop stress from initial compression to tension in the surface layer of particles. Both in situ and ex situ experiments have revealed the sharp a-Li$_x$Si/c-Si interface (ACI) of ~1 nm thickness developed during the lithiation of Si.[15,30,31,34,88] Progressive migration of the ACI leaves a thickening a-Li$_x$Si shell in its wake. In such a two-phase lithiation mode, the Li concentration gradient is large across the narrow ACI, i.e., from x ~ 0 on the c-Si side to x ~ 3.75 in the a-Li$_x$Si shell. Consider a representative material element A in the surface of a Si nanoparticle, the direct lithiation of element A, while being swept by the lithiation front, results in the initial hoop compression due to the constraint of surrounding materials. However, continuous lithiation and associated volume expansion at the moving reaction front push out the lithiated shell. Analogous to the development of tensile hoop stress in the inflating balloon, the stress state in element A will be reversed from compression to tension. As a result, surface cracks may nucleate from the outmost a-Li$_x$Si shell with the largest tensile hoop stress and propagate inwards as more lithiated alloys are being pushed out.

Such hoop stress reversal is not predicted by a single-phase model in which the compression in the lithiated shell is maintained by continuous Li insertion. The inner c-Si core is thought to experience tensile stress build-up and eventually cracks. Such central-cracking scenario is observed in neither Si nanowires nor nanoparticles experiments due to the two-phase, rather than the single-phase structure present in the experiments.[15,30,31,88] We have always observed crack nucleation from the lithiated surface (Figure 9a), but never from the c-Si core during lithiation. It should be emphasized that the hoop stress development and surface cracking are related to the spherical curvature; as for a planar ACI on a Si foil, cracking of the c-Si are observed to nucleate from the ACI and propagate into c-Si due to the tensile stress. Also, while the hoop tension tends to initiate surface cracks, the small-sized nanoparticles nevertheless avert fracture. This is because the stored elastic strain energy from the electrochemical reactions is not enough to drive crack propagation, as dictated by the interplay between the two length scales, i.e., particle diameter and crack size, that control the fracture.[15,34]

REVIEW

3. Carbonaceous Nanomaterials

3.1. Lithium Embrittlement of Carbon Nanotubes: Chemical or Geometrical Origin?

Due to their excellent physical properties such as superior electrical conductivity and high mechanical strength, carbon nanotubes (CNTs) are being extensively studied as a promising anode material for LIBs.[89–98] It has been reported that the reversible capacities of single-walled carbon nanotubes (SWCNTs) and MWCNTs are 450-600 mAh/g[90,92] and up to 1000 mAh/g,[91] respectively, which are much larger than graphite. It is expected that the CNT-based electrode should have a much longer cycle lifetime than other anode materials, as it can benefit from the mechanical flexibility and robustness of the CNTs. However, it is found that the MWCNTs become very brittle upon lithium insertion, which is attributed to the lithiation-induced embrittlement effect.[38]

Figure 10a shows the TEM image of a pristine arc-discharged MWCNT with diameter about 20 nm, showing the straight tube structure and clean surface. A layer of Li_2O was formed on the surface of the MWCNT during lithiation (Figure 10b), and the thickness of the Li_2O layer increased with further lithiation (Figure 10c-d). After delithiation, the thickness of this surface Li_2O layer did not show obvious shrinkage (Figure 10e). This stable Li_2O layer is likely related to the formation of the
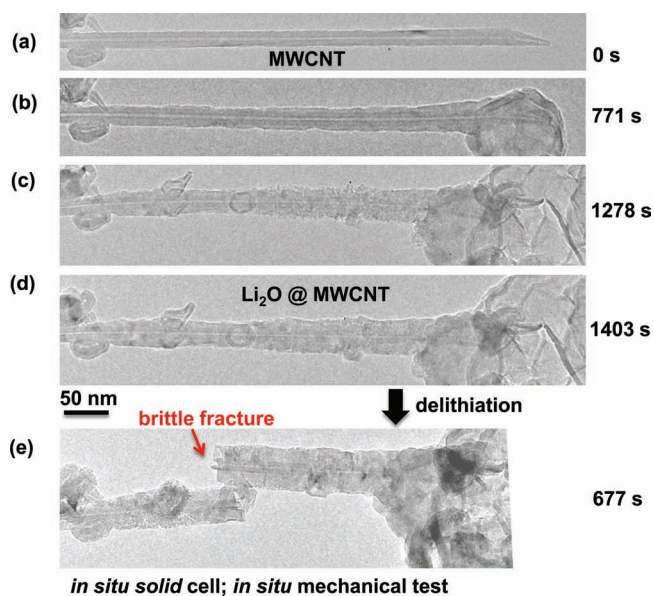

Figure 10. Brittle fracture upon compression of an arc-discharged multi-walled carbon nanotube (MWCNT) after a lithiation-delithiation cycle. (a-d) Time-lapse TEM images showing the structure evolution of an arc-discharged MWCNT upon lithiation. (a) A pristine MWCNT with diameter about 20 nm, showing the straight tube structure and clean surface. (b) Upon lithiation, a uniform Li_2O layer was coated on the surface. (c,d) The thickness of the surface Li_2O layer increased as lithiation continued. (e) Brittle fracture upon compression of the MWCNT after delithiation, showing a sharp fracture surface. The thickness of the surface Li_2O layer did not change much during cycling, which is consistent with the reported large irreversible capacity due to the solid electrolyte interface (SEI) formation in the conventional electrochemical cells.

SEI layer in the conventional electrochemical cells, and is consistent with the reported large irreversible capacity due to the SEI formation in CNT-based LIBs.[93–95,99] Brittle fracture of the MWCNT with a sharp edge was observed (Figure 10e), which is strikingly different from the 'sword-in-sheath' failure mode of pristine MWCNTs.[100,101]

Consistent with the in situ TEM observations, the brittle fracture of MWCNTs was also found in conventional electrochemical cells after multiple cycles.[38,102–103] As shown in **Figure 11**a, the surface of the MWCNT was coated with an SEI layer after cycling in a conventional electrochemical cell using an EC/DMC electrolyte. The MWCNTs broke with sharp fracture edges under compression (Figure 11a), same as that observed in the in situ TEM test (Figure 10e), suggesting the lithiation-induced embrittlement of MWCNTs. Besides our in situ and ex situ experiments, Masarapu et al. reported that MWCNTs were broken into smaller pieces after 2000 cycles (Figure 11b),[102] and similar brittle fracture of CNTs was also observed after 200 deep lithiation-delithiation cycles by Pol et al. (Figure 11c).[103] These ex situ reports agree well with our results from in situ TEM electrochemical study, indicating the methodology of in situ TEM electrochemistry is suitable for studying the fundamental science relevant to real LIBs.

Ab initio tensile simulation of double-walled carbon nanotube (DWCNT) has been performed.[38] We constructed the simulation model with (5,5) and (10,10) armchair-type CNTs for the inner and the outer tube, respectively. A 23.6 Å × 23.6 Å × 4.93 Å simulation cell including 120 carbon atoms were used with the axis along z direction. 9 Li atoms were randomly inserted one by one between the two walls to obtain the lithiated DWCNT. The tensile strain was applied to the model by elongating the simulation cell along z direction. After the each increment of the strain, the structural optimization was performed while fixing the cell size. Similar procedures were employed to evaluate the effect of Li insertion on the mechanical properties of the different materials shown in this review. **Figure 12**a shows the stress-strain curve of the DWCNT with and without Li between the walls. The fracture strain of the lithiated DWCNT was reduced to 19% from 29% of that in the pristine tube. The lithiation reduced the fracture strain by 34%. Such weakening is attributed first to the insertion of intertubular Li atoms causing the development of hoop tension in the circumferentially closed tube walls. This is manifested by the measured 6% inter-tube distance increase in the absence of applied mechanical loading, that corresponds to ~50 GPa residual tensile hoop stress.[38] Furthermore, during subsequent axial loading, due to the Poisson contraction effect, the intertubular Li atoms produce additional "point force" to further embrittle the CNTs.[38] Because of the topological constraint of the tube wall to form a closed circle, lithiated or not, axial tension causes the radial contraction of the CNT. As a consequence of the residual hoop tension, estimated to approach ~50 GPa after lithiation before axial tension, plus the Poisson contraction effect after external axial tension is applied, the intertubular Li is pushed against the walls. This "point force" effect gradually emerged and localized the deformation as the axial tension increased as shown in Figure 12b.[104,105] Firstly, the Li atoms were pushed into the inner wall due to the compression from the outer wall, leading to the large elongation of the

www.MaterialsViews.com

ADVANCED
ENERGY
MATERIALS
www.advenergymat.de

REVIEW
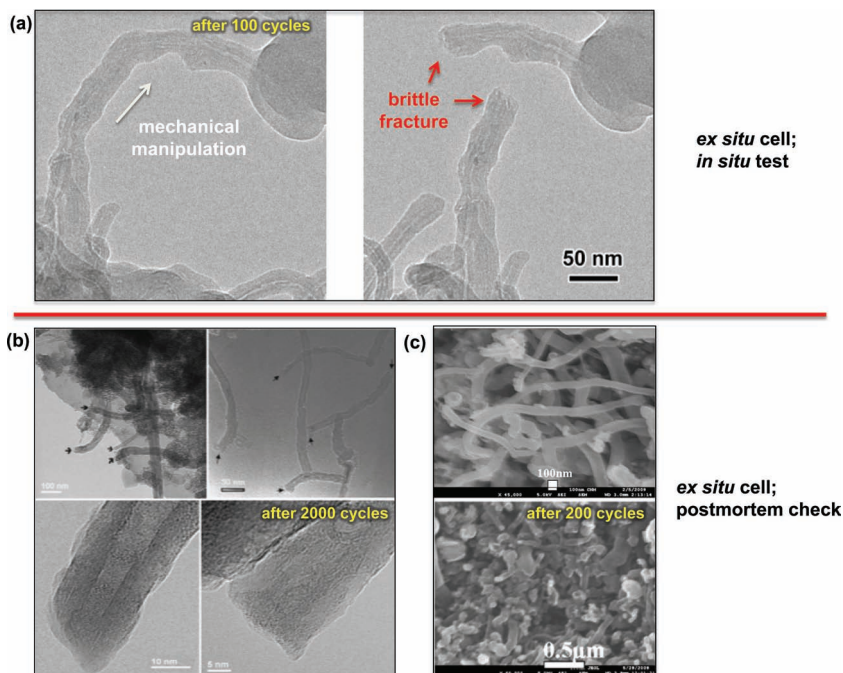
Figure 11. Brittle fracture of MWCNTs after multiple cycles in conventional ex situ electrochemical cells. (a) Brittle fracture of a MWCNT after 100 cycles in a Swagelok cell. Left: morphology of a MWCNT after 100 cycles; Right: brittle fracture of the MWCNT resulting in a flat edge under in situ compression. (b) TEM images showing broken MWCNTs with flat edges after 2000 charge-discharge cycles. (c) SEM images showing the brittle fracture of the MWCNT electrode after 200 deep discharge cycles. Bottom: The MWCNTs were broken into smaller fragments, which was significantly smaller than the average length of the parent nanotubes (Top). Reproduced with permission.[38,102,103] Copyright 2011, American Chemical Society; Copyright 2009, Wiley; Copyright 2011, the Royal Society of Chemistry.

C-C bonds adjacent to the Li atoms. This corresponds to the first stress drop after the stress reaching its maximum at the strain of 19%. Then the outer tube was fractured from the point where the wall was pushed against the intertubular Li atoms at the strain of 25% corresponding to the second stress drop.

The simulation results imply that the hoop stress and "point force" from the Li atoms caused the local bond breaking that further triggered the brittle fracture of CNT as observed in the experiments.[38] The generation of this "point force", however, can have a nonlocal geometrical origin due to the circumferentially closed tube walls of the MWCNTs that gives rise to (a) residual hoop tension after lithiation, as well as (b) additional Poisson contraction in response to external axial tension. Since the carbon-carbon bonding chemistry and carbon interaction with lithium should be local and largely the same between MWCNTs and graphene nanoribbons (GNRs), a comparison with GNRs would allow us to further pin down the origin of lithium embrittlement: if the lithium embrittlement behavior is similar between MWCNTs and GNRs, then it can have a local, chemical origin. But if the

lithium embrittlement behavior is dissimilar, the embrittlement of MWCNTs may have a nonlocal geometrical or mechanical origin, related to the nonlocal generation of the hoop stress and "point force". Such experimental checks have indeed been performed using our in situ platform, to be detailed next.

3.2. Graphene as a Robust Anode Material

Few-layered graphene nanoribbons (GNRs) were studied with the lithiation and mechanical tests similar to those for MWCNTs.[39] Compared to the tubular structure of MWCNTs, the GNRs consisted of about 5 ~ 10 layers of planar graphitic sheets. During lithiation, the spacing of these sheets (the basal planes) increased from 3.4 Å to about 3.6 Å, corresponding to an expansion of about 6% and consistent with the <10% volumetric change of intercalated graphite.[43] Similar to the MWCNTs, thick Li_2O layers were wrapping the GNRs. However, the GNRs showed high robustness in the following mechanical manipulation (**Figure 13**). Unlike the embrittled MWCNTs, lithiated GNRs survived in the repeated compression/release cycles without fracture, and they even recovered the original shape, indicating insignificant residual deformation (Figure 13a-c).

Figure 13d shows the tensile stress-strain curves for the pristine graphene, C_6Li graphene, and C_6Li graphite in the zigzag and the armchair directions. The ideal strength of the pristine graphene was 112 GPa at 19% strain and 121 GPa at 24% strain for the zigzag and the armchair direction, respectively. When Li is added, they were reduced to 98 GPa at 18% strain (zigzag) and 109 GPa at 20% strain (armchair). The decrease of the fracture strain upon lithiation is 5% ~ 14% in the graphene, which
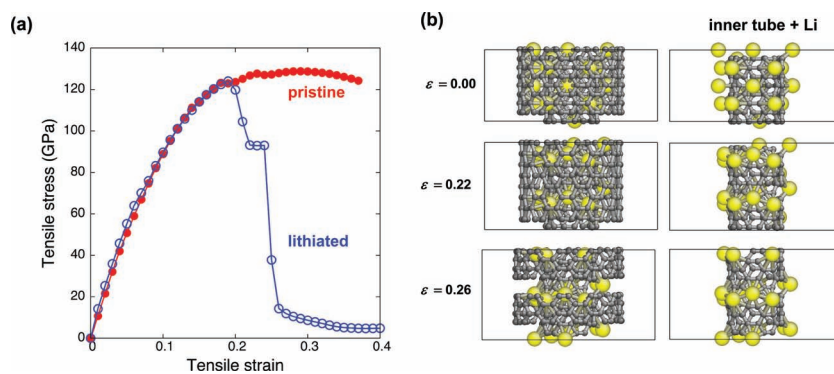
Figure 12. Simulations showing embrittlement of a double-walled CNT after lithiation. (a) Simulated stress-strain curves of an axially strained CNT before (red trace) and after lithiation (blue trace). The lithiated CNT shows brittle fracture under tensile stress. (b) Atomic structures at different strain level showing the fracture of the outer tube, consistent with the experimental observations.

REVIEW

ADVANCED
ENERGY
MATERIALS
www.advenergymat.de

Materials
Views
www.MaterialsViews.com
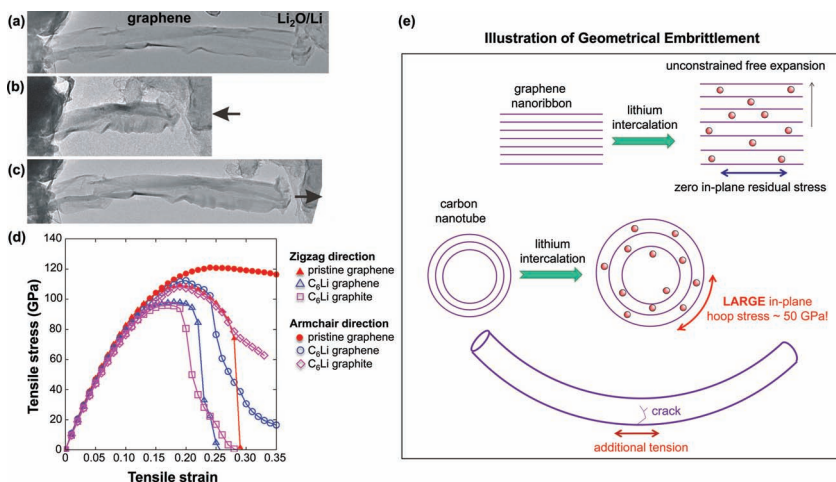
Figure 13. Mechanical robustness of graphene after lithiation. (a) Pristine graphene in contact with the Li$_2$O. (b,c) The lithiated graphene was compressed (b) and released (c), showing great flexibility and no fracture. (d) Simulated stress-strain curves showing similar mechanical property of graphene and graphite under tensile stress along both the zigzag and armchair directions, suggesting superb mechanical stability of graphene even after being lithiated. (e) Illustration of geometrical embrittlement effect in MWCNTs, but not in multi-layered GNRs. Reproduced with permission.[39] Copyright 2012, Elsevier.

is insignificant compared to the DWCNT (Figure 12a). Furthermore, the result of the lithiated bulk graphite (infinite stack of graphene layers) showed almost the same strength and the fracture strain as the lithiated graphene. This indicates the interlayer interaction is negligible in the graphite and the number of the graphite layers has no effect to the strength reduction upon lithiation. Thus, there does not seem to be a significant "chemical embrittlement" effect, in the sense that the C-C bond network common in both graphene and MWCNT does not seem to be directly weakened chemically by the insertion of lithium. On the other hand, the MWCNTs showed significant lithiation-induced embrittlement. As discussed earlier,[38] such embrittlement is attributed to the residual hoop stress of ~50 GPa caused by the intertubular Li atoms in the circumferentially closed tube walls, in conjunction with the additional Poisson contraction upon external loading, that sums to the "point force", and which is expected to become insignificant in the "flat" graphene and the graphite.[106,107] And indeed, lithiation-induced embrittlement was not observed either in graphite or in graphene. This indicates the structurally constraining effect of CNTs, that is, the nonlocal geometrical requirement of maintaining a circumferentially-closed circle, plays a dominant role in the embrittlement, as opposed to the chemical effect such as charge transfer due to the lithiation. This is termed "geometrical embrittlement".[38]

These results show great promise of graphene as a robust battery material (due to the lack of circumferential constraint) with high electronic conductivity, mechanical stability, and huge specific surface area. Indeed, depending on the synthesis and test method, graphene has shown high capacities in the range of 540 ~ 1264 mAh/g.[108] The comparative in situ lithiation studies on MWCNTs and GNRs also indicate that the property is closely related to the structure (geometric constraints), which in turn partially explains the relatively large variation in measured capacity of graphitic materials in the literature.[108,109]

4. Oxide Nanowires

Some oxide nanowires (ZnO) also show significant lithium embrittlement,[40] while others (SnO$_2$) do not.[13] In contrast to carbonaceous materials in Section 3 where a significant "geometrical embrittlement" effect was identified, here we have found a significant "chemical embrittlement" effect.

## 4.1. Leapfrog Cracking and Nanoamorphization of ZnO Nanowires

While the lithiation proceeded in a continuous manner in most of the nanowires we examined,[13,31,36,37] the reaction front did not move continuously in ZnO nanowires.[40] Instead, it leaped forward by initiating discrete cracks before the reaction front (**Figure 14**a), followed by rapid Li$^+$ surface diffusion and inward amorphization. The cracks divided the single-crystalline ZnO nanowire into multiple segments, which were then lithiated individually. When two growing amorphous zones came into contact, they formed a new interface. This is a glass-glass interface (GGI), as the two glassy domains were developed separately with discontinuous atomic structures when they met and adhered. Thus, the lithiated ZnO nanowire can be referred to as "nanoamorphous" or "nanoglass", since it contains multiple discontinuous glassy domains.[110]

The GGIs left jagged reliefs on the nanowire surface. They also remained at the same locations during multiple charge/discharge cycles afterwards, which we call the "GGI memory effect". Thus the damages trapped in the GGIs during the first lithiation can be permanent and affect the battery lifetime. In fact, ZnO is known to have poor cyclability. On the other hand, lithiation of SnO$_2$ features continuous front propagation, a single amorphous domain with smooth surface, and involves no crack formation during lithiation but plenty of gliding dislocations[13,42], indicating good plasticity. It therefore should not be too surprising that macroscopically, SnO$_2$ shows better cyclability than ZnO electrodes.[111,112] One may conjecture that certain microscopic mechanism greatly affects the difference in durability of these two oxide electrode materials.

4.2. Lithium Embrittlement: Chemical Effects

The cracking of ZnO nanowires cannot be explained simply by the volume expansion during lithiation, because there was no cracking in the pristine crystalline materials during lithiation of other nanowires with even larger volume expansions such as SnO$_2$ and Si.[13,31] Although Si nanowires show nearly 300% volume expansion after lithiation, no sign of the crack formation was observed in the crystalline segment located in front of the reaction front. The chemical nature of Li-Zn interaction must play a role. Similar to hydrogen embrittlement, previous studies have shown the presence of Li can weaken the materials,

Makerials
Views
www.MaterialsViews.com

ADVANCED
ENERGY
MATERIALS
www.advenergymat.de

REVIEW
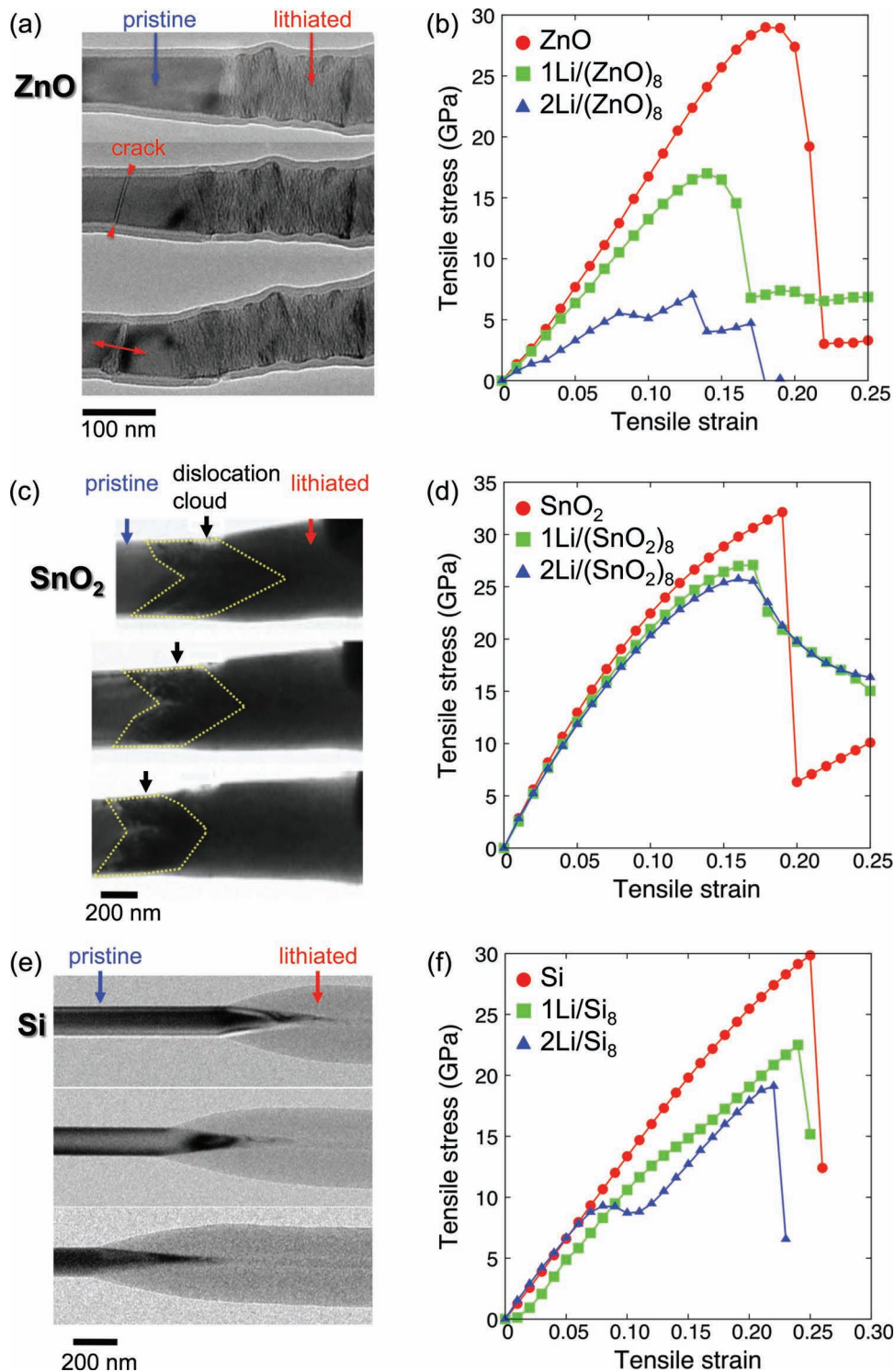
Figure 14. Comparison of the microstructural evolution and mechanical stability of ZnO, SnO₂, and Si nanowires upon lithiation. (a) Discrete cracks formed before the reaction front of a ZnO nanowire followed by axial lithiation of the isolated ZnO crystals between the cracks. (b) Simulated stress-strain curves showing significantly reduced strength of ZnO upon Li insertion. (c) High density dislocation region ("dislocation cloud") formed at the reaction front of a SnO₂ nanowire as the structural precursor of amorphization. (d) Simulated stress-strain curves showing less influence of Li insertion on the strength of SnO₂ than ZnO. (e) Two-phase manner of Si lithiation by migration of an atomically sharp interface between the unreacted crystalline Si and lithiated a-Li$_x$Si. (f) Simulated stress-strain curves showing little change in mechanical property of Si upon Li insertion. Reproduced with permission.[13,31,40] Copyright 2011, the American Chemical Society; Copyright 2010, the American Association for the Advancement of Science.

known as lithium embrittlement.[26,113–116] To elucidate the effect of Li on strength and ductility, we conducted ab initio tensile decohesion simulations for ZnO, SnO₂, and Si nanowires. The theoretical results and the corresponding experimentally observed reaction mechanisms are presented in Figure 14. The simulations were conducted at the low Li concentration, corresponding to the early stage of lithiation.

The lithiation of the ZnO nanowire proceeds by the discrete crack formation as shown in Figure 14a. Figure 14b shows the tensile stress-strain curve for ZnO at different Li concentrations. The ideal strength of the pure ZnO was 29 GPa. When Li was added, it decreased to 17 and 7 GPa for $1Li/(ZnO)_8$ and $2Li/(ZnO)_8$, respectively. In contrast, in SnO₂ glissile dislocations were seen to be generated and propagated along the nanowire axis at the reaction front, transforming the initial crystalline structure to an amorphous matrix (Figure 14c). The calculations for SnO₂ shown in Figure 14d revealed that the effect of Li on the tensile decohesion is much smaller compared to the ZnO at the same Li concentration. These results indicate that the lithium embrittlement appears to be more severe in ZnO than in SnO₂. We attribute this difference to the aliovalency of Sn cations; both Sn(IV) and Sn(II) are the frequently observed electronic valence state of Sn, while Zn is dominated by Zn(II). Thus, Sn can gradually adapt to the electronic-structure change when Li atoms are inserted and start to reduce Sn(IV) in SnO₂, while ZnO has no such option but to break the Zn-O bond.

Neither cracks nor dislocations were observed in the c-Si segment during the lithiation of Si nanowires (Figure 14e). In the simulation of Si, the strength reduction is 24% and 37% at $1Li/Si_8$ and $2Li/Si_8$, respectively. Such direct lithium embrittlement in Si is more significant than SnO₂, but less severe than ZnO. In $2Li/Si_8$ configuration, a slight stress drop took place at 9% strain. At this point, the Si-Si bond in the vicinity of Li was stretched more compared to other Si-Si bonds. This is due to the weakening effect of Li insertion caused by local electronic structure modification. However, this drop did not lead to a complete fracture of the Si. Although the local Si-Si bond near the Li was weakened, other Si-Si bonds remain largely intact, serving to maintain the structure integrity. Therefore, the model material was able to accommodate further tensile deformation at this Li concentration.

Although the possibility of lithium embrittlement was speculated in LIBs from the observation of the lithium battery leakage,[29] there has been no extensive research in this direction. Our findings shed light on the importance of nanocracking and lithium embrittlement in LIB electrode since they are integral to both lithiation and battery decrepitation mechanisms. Our work showed two mechanisms of Li embrittlement, namely local, chemical versus nonlocal, mechanical effects. The inserted Li atoms alter the electronic structure of the matrix and weaken the interatomic bonds to reduce the strength (chemical effect). The magnitude of the effect differs due to the aliovalency and the bonding nature of the host material. Thus, the occurrence of the lithium embrittlement is highly material dependent. However, lithium embrittlement may not be universally explained by the chemical effect. As shown in the previous section, lithium embrittlement occurred in MWCNTs, but not in GNRs. Clearly, the topological constraint of the nanotubes, that is, the geometrical requirement of maintaining a circumferentially-closed

circle, lithiated or not, played an important role in the Li embrittlement susceptibility as well, due to nonlocal generation of "point force", residual plus induced. These results suggest that both chemical and structural effects should be carefully analyzed to understand the lithiation-induced embrittlement of the LIB electrode materials, which is crucial for predicting electrode degradations.

## 5. Al Nanowires and Al₂O₃ Coatings

5.1. Pulverization of Al Nanowires

The insertion/extraction of a large amount of lithium in the active materials can induce buildup of large mechanical stresses that can further cause pulverization leading to the loss of electrical contact and capacity fading after a few cycles.[43,117–123] We have used the in situ TEM electrochemistry to study the pulverization processes by taking the Al nanowire as a model system.[37] **Figure 15**a shows a pristine Al nanowire with uniform contrast and a uniform diameter of about 40 nm. After lithiation, the nanowire swelled and elongated (Figure 15b). Voids nucleated and formed at the first delithiation stage, as marked by red arrow in Figure 15c. The nanowire was pulverized to isolated Al nanoparticles after 4 cycles of lithiation and delithiation (Figure 15d). Figure 15e shows an enlarged image of the voids between the nanoparticles. From the in situ TEM observations, it is clear that the formation and growth of the voids only occurred at the delithiation stage because of the dealloying of lithium from the LiAl alloy, eventually giving rise to pulverization of the metallic nanowire electrode.

Conventional electrochemical cycling experiments on the Al nanowires were also carried out using commercial liquid electrolyte with LiPF₆ dissolved in an EC/DMC mixture. The voltage profile and specific capacity of galvanostatic cycling at 1C rate are shown in Figure 15f and g, respectively.[37] The capacity loss began immediately during the first delithiation and only occurred at each delithiation step. It is also worth noting that the capacity of lithiation is about the same as that of the previous delithiation. This is consistent with the *in situ* TEM observations that the pulverization only occurs during delithiation and leads to loss of connectivity and conductivity of the electrode materials, which eventually causes capacity fading.

5.2. Coatings

In the past decade, various kinds of metal oxides,[124–126] such as Al₂O₃,[127–132] Co₃O₄,[133] ZrO₂,[134,135] TiO₂,[136,137] MgO,[138–140] ZnO,[141] and SnO₂[142] have been studied as coatings on active materials for improving the battery performance. Among these metal oxides, Al₂O₃ has been extensively explored. It has been shown that a thin Al₂O₃ coating layer on active materials, such as LiCoO₂ and LiMn₂O₄,[143,144] can enhance the cycling performance. Recently, atomic layer deposition (ALD), as a gas-phase method of thin-film growth with conformal coating and atomic thickness control, has been employed as a coating method for LIBs. Ultrathin ALD coated Al₂O₃ layer has been

www.MaterialsViews.com

ADVANCED
ENERGY
MATERIALS
www.advenergymat.de

REVIEW
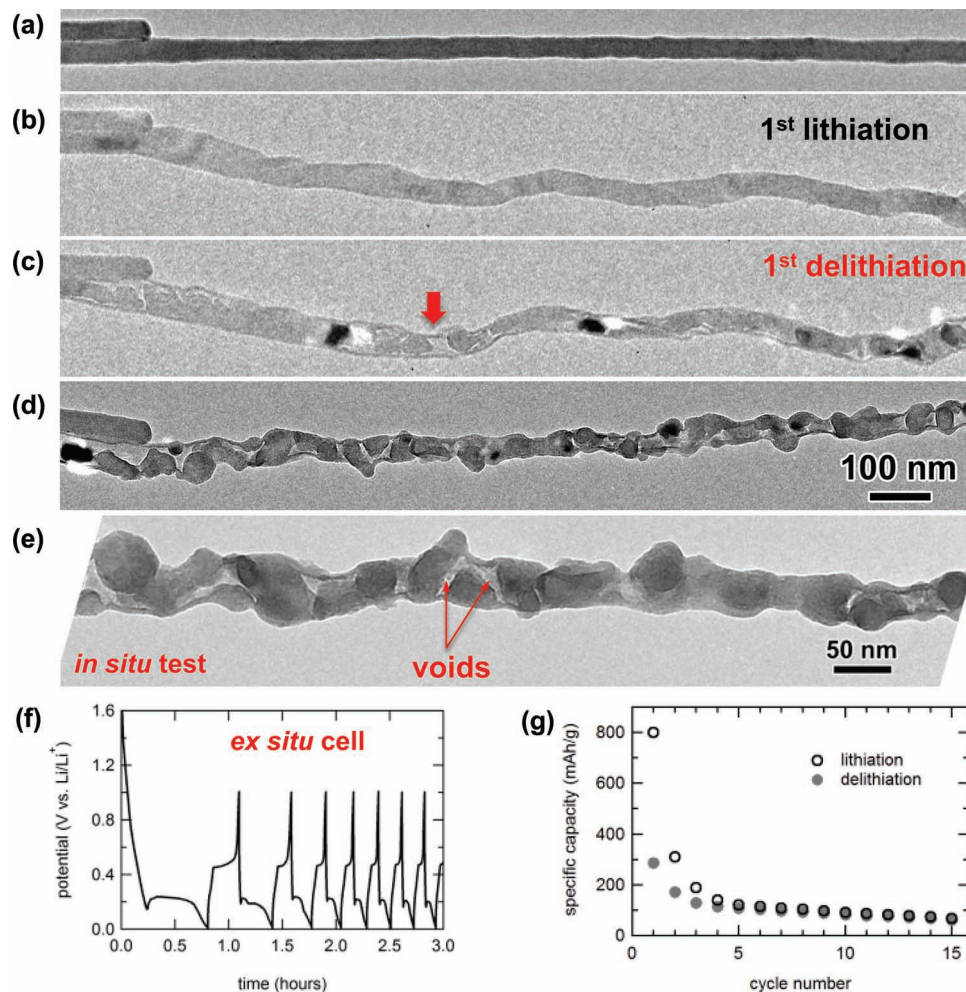
Figure 15. Pulverization of Al nanowire during electrochemical cycling. (a) Pristine Al nanowire with uniform diameter and contrast. (b) Morphology after the first lithiation process, showing the volume expansion in both radial and axial directions. (c) Voids formation after the first delithiation process. The red arrow marks one of the voids. (d,e) Pulverized Al nanowire consisting of isolated Al nanoparticles after 4 lithiation-delithiation cycles. (e) Enlarged image clearly showing the voids between the particles. (f) Voltage profile of the Al nanowire assembles cycled at 1C rate in the ex situ electrochemical test. (g) Capacity retention of the Al nanowires as a function of cycle number. Capacity loss occurs during delithiation, while lithiation capacity is about the same to the previous delithiation capacity. Reproduced with permission.[37] Copyright 2011, the American Chemical Society.

reported to improve the durability and rate capability of the LiCoO$_2$ cathode,[143–145] and the cyclability of amorphous Si anode.[146] However, the underlying mechanisms as well as the morphological and compositional evolution of these coatings during cycling were not clear.

In situ TEM electrochemical study opened opportunities for understanding the morphology and composition changes of the ultrathin surface coating at the atomic scale. The Al nanowire with a naturally oxidized surface layer of Al$_2$O$_3$ (about 4–5 nm) was used as a model system (**Figure 16**).[37] Combining the TEM images and the elemental mapping results, the morphology and composition changes can be tracked for both the coating layers and the active materials. As shown in the inset images in Figures 16a and b, the surface Al$_2$O$_3$ layer first underwent lithiation. Then the inner Al core was lithiated following lithiation of the Al$_2$O$_3$ surface layer (Figure 16c). The Al nanowire was pulverized to generate isolated Al nanoparticles after one

lithiation-delithiation cycle. Surprisingly, an intact tube, which was converted from the surface Al$_2$O$_3$ layer, confined the pulverized Al nanoparticles, maintaining the integrity of the electrode (Figure 16d). The zero-loss image shows the pulverized nanoparticles enclosed by a tube formed on the nanowire surface after 3 cycles. The electron energy loss spectroscopy (EELS) map of Al element matches well with the enclosed nanoparticles in the zero-loss image, indicating the nanoparticles in the tube were Al nanoparticles. Based on the EELS maps of the Li, Al and O elements, it can be concluded that the surface Al$_2$O$_3$ layer has evolved into a Li-Al-O glass layer (Figure 16e). This Li-Al-O glass tube survived the 100% volume expansion occurred during the lithiation of the inner Al nanowire, showing the exceptional mechanical robustness. In addition, the Li ion conductivity of the Li-Al-O glass is up to the order of 10^{-6} S/cm at room temperature,[147] indicating that the formed Li-Al-O glass tube served as a good solid electrolyte for Li ion transport.
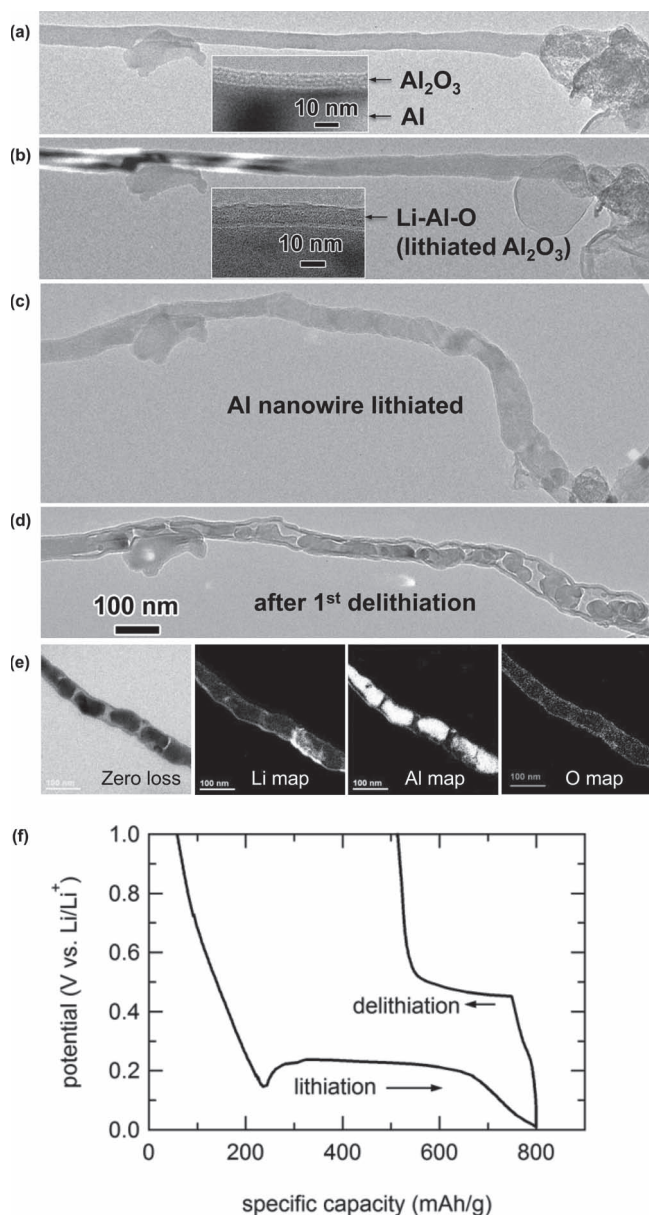
Figure 16. Evolution of an Al_2O_3 surface layer to the Li-Al-O glass layer. (a–d) In situ electrochemical test of an Al nanowire with a native Al_2O_3 surface layer. (a) Pristine Al_2O_3/Al nanowire. The inset high-magnification image shows the amorphous Al_2O_3 coating on the Al nanowire. (b) Initial stage of lithiation showing that the Al_2O_3 surface layer was lithiated first. The inset shows a high-magnification image of the lithiated Al_2O_3 layer that was converted to a Li-Al-O glass tube with increased thickness. (c) The Al core was lithiated after lithiation of the Al_2O_3 surface layer. (d) Morphology of the nanowire after one lithiation-delithiation cycle. The inner Al wire was pulverized, but the outer lithiated layer formed a continuous tube enclosing the pulverized Al wire, keeping the integrity of the electrode. (e) Zero loss image and electron energy loss spectroscopy (EELS) maps of Li, Al and O elements of an Al nanowire after 3 cycles, indicating a structure of discrete Al nanoparticles wrapped by a continuous Li-Al-O tube converted from the native Al_2O_3 layer. (f) Voltage profile as a function of capacity in the initial cycle of Al nanowire assembles in the ex situ cell. The large sloping voltage during lithiation is attributed to the irreversible lithiation of Al_2O_3, and the following plateau at ~ 0.2 V corresponds to lithiation of Al. The delithiation process shows large capacity loss, probably due to the pulverization. Reproduced with permission.[37] Copyright 2011, the American Chemical Society.

It is noted that even after the Al nanowire was pulverized to separated particles after delithiation, lithiation/delithiation could still continue to occur to some extent.[37] We suggest that this is because the electrical connectivity was not completely lost after pulverization. Some isolated particles indeed became "dead" after fracture, which is also proven by the ex situ cycling data showing decreased capacity after each delithiation (Figure 15f-g).[37]

The ex situ cycling data agree well with the in situ TEM observations and reinforce the conclusions drawn above. Figure 16f shows the voltage profile as a function of charge capacity for the initial cycling of Al nanowire assemble sample in the conventional electrochemical cell. The initial sloping high voltage is attributed to the irreversible lithiation of Al_2O_3 shown in Figure 16b, while the relatively stable voltage near 0.2 V corresponds to lithiation of Al metal as shown in Figure 16c. Delithiation occurs at approximately 0.5 V and shows an enormous loss of capacity in the first cycle, indicating the pulverization of Al nanowires during delithiation (Figure 16d).

The formation of mechanically robust Li-Al-O glass tube due to lithiation of Al_2O_3 provides important insights into the recent findings that an ALD-grown thin layer of Al_2O_3 on active electrode materials can increase the cycle lifetime of the corresponding electrodes dramatically. **Figure 17** shows the results of improved performance of electrodes coated with thin films in the ex situ experiments. Figure 17a shows the TEM image of $LiCoO_2$ particles coated by 6 ALD cycles of Al_2O_3, and the cycling performance was greatly improved with respect to the uncoated bulk- and nano-$LiCoO_2$ samples (Figure 17b). The uncoated bulk-$LiCoO_2$ electrode showed rapid capacity fading in a few cycles, and the bare nano$LiCoO_2$ electrode showed the delayed decay of capacity. The Al_2O_3-coated nano-$LiCoO_2$ electrode showed stable capacity retention in 200 cycles.[143] Besides the application of an Al_2O_3 coating on cathode materials, it was also reported that the Al_2O_3 coating on anode materials, such as Si,[146] can improve the cyclability of the LIBs. Figures 17c and d compare the surface morphology of Si and Al_2O_3 coated Si thin film electrodes after 11 cycles. The Al_2O_3 coated Si (Figure 17c) shows much less cracks than the uncoated sample (Figure 17d), indicating the Al_2O_3 coating suppresses the mechanical degradation of the Si anode. The depth profile of the different Al compound ratio is shown in Figure 17e, indicating the presence of $LiAlO_2$ on the top surface layer, which can provide a facile Li-ion transport path.[148] This result is consistent with our in situ observations.[37]

From the above in situ and ex situ results, it can be concluded that the performance improvement of LIBs using the Al_2O_3 coating on active materials is attributed to the formation of the Li-Al-O glass layer, which has two major effects: (1) The Li-Al-O glass layer acts as an artificial SEI layer, which can provide good Li-ion conductivity; (2) The robust Li-Al-O glass layer can mitigate loss of mechanical contact of the active materials, so as to prevent them from breaking off from the electrodes.

6. In Situ Chemical Lithiation

As described above, in situ electrochemical experiments of various materials have yielded many insightful results that are consistent with corresponding ex situ tests using conventional

Materials Views

www.MaterialsViews.com

ADVANCED
ENERGY
MATERIALS
www.advenergymat.de

REVIEW
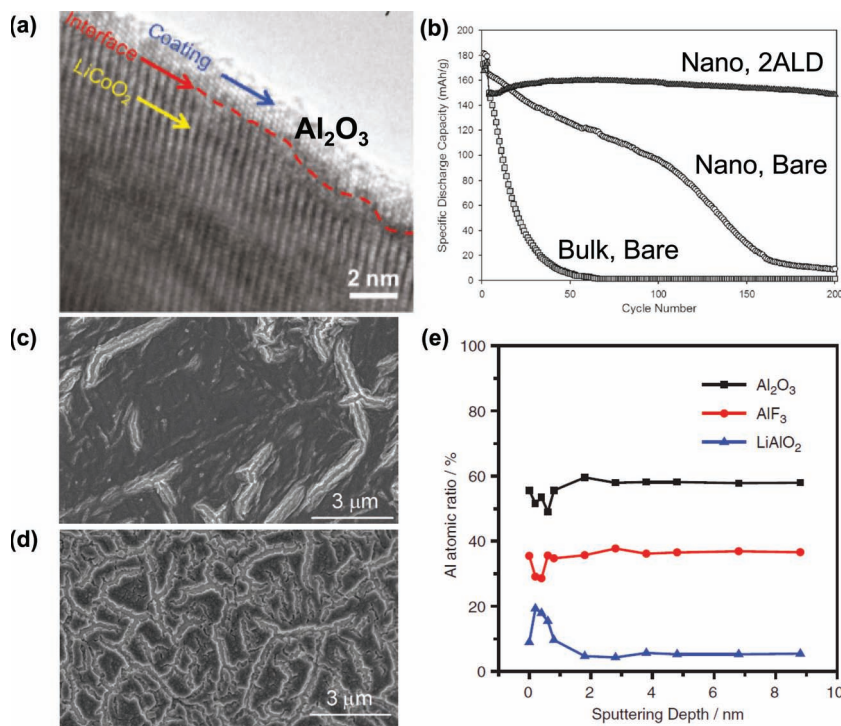
Figure 17. Improved cyclability of nanoLiCoO$_2$ cathode coated with an ultrathin Al$_2$O$_3$ layer (a,b) and the functions of ultrathin Al$_2$O$_3$ layer on amorphous Si anode (c–e). (a) High resolution TEM image showing the LiCoO$_2$ surface was coated with Al$_2$O$_3$ by 6 atomic layer deposition (ALD) cycles. (b) Comparison of the cycling performance of three electrodes. The uncoated bulk- and nanoLiCoO$_2$ electrodes showed rapid or delayed capacity fading, respectively, while the Al$_2$O$_3$-coated nano-LiCoO$_2$ electrode showed stable capacity retention in 200 cycles. (c,d) SEM images showing the surface morphology of Al$_2$O$_3$ coated Si (c) and bare Si (d) thin film electrodes after 11 cycles. (e) The depth profile of the different Al compound ratio, indicating the presence of LiAlO$_2$ on the top surface. Reproduced with permission.[143,148] Copyright 2011, the American Chemical Society and Wiley.

electrochemical cells. A general observation is that the electrochemical reactions and mechanical responses, particularly the phase transformations and deformation modes, are highly specific to the material itself, and are less sensitive to the experimental procedures. This suggests that a controlled chemical reaction between Li and M (denoting the material of interest) will likely generate useful information of the lithiation mechanism. On the other hand, in situ TEM electrochemistry usually requires special instrumentation to complete positioning and biasing, which may not be accessible in a conventional TEM. Here we describe an *in situ* chemical lithiation method that can be used for fast screening of the lithiation-induced phase transformation and deformation.

Li$_2$O, as well as many other Li-containing compounds, decomposes into elemental Li and volatile gas under electron beam irradiation of high energy and high dosage rate (~100 A/cm^2 in our experiments).[34,149,150] The electron beam induced decomposition of Li$_2$O can be utilized for in situ chemical lithiation. As shown in **Figure 18**a, Li metal can be scratched with a conventional 3-mm TEM grid made of Cu, Ni, or Mo, and there will be a native Li$_2$O layer grown on Li metal in the dry air with minimum moisture. Nanomaterials such as nanoparticles or nanowires can be dispersed onto the Li$_2$O/

Li-loaded TEM grid. Due to the insulation of Li$_2$O, the nanomaterial remains unlithiated before observation. The electron beam acts as a shutter to control the onset of lithiation, and the mechanism can be described as following: (1) generation of Li under electron beam: 2Li$_2$O → 4Li + O$_2$↑; (2) in situ chemical lithiation: x Li + M → Li$_x$M. As a demonstration, SnO$_2$ nanowires can be readily lithiated with the similar microstructural evolution as that observed in the in situ electrochemical lithiation experiment,[13] such as amorphization, volume expansion, and high density of mobile dislocations at the reaction front (Figure 18b-d).

The driving force of the chemical lithiation is the negative Gibbs free energy of the reaction, underlying the high reactivity of elemental Li. Compared to the well-controlled electrochemical lithiation, it certainly has some limitations, such as lacking the capability of delithiation and manipulation. The reaction products, kinetics, and thermodynamics in a chemical lithiation process could be very different from those in the electrochemical process. Therefore one should be cautious in extrapolating the chemical lithiation data to explaining the electrochemical lithiation. However, chemical lithiation offers opportunities of fast screening of materials of interest without a special TEM holder, such as Nanofactory TEM-scanning tunneling microscopy (STM) holder.[13,15,30,31,35,36,38,40–42] It can be easily conducted in the conventional TEM configuration, or in a scanning electron microscope (SEM) to allow 3D observations. Particularly, it facilitates the study of nanoparticle lithiation, because the mass of the active material is small. As we have observed in the preliminary experiments, the chemical lithiation processes became slower and finally stopped during long-lasting experiments, which was likely limited by Li transport along the long wires. We also found that when the electron beam is moved away from the Li$_2$O, the chemical lithiation stops due to the lack of continuous Li supply. It should be mentioned that in our solid cell nano battery setup, Li$_2$O was used as a solid electrolyte.[15,30] During cycling of the solid cell, the Li$_2$O remained stable with no electron-beam-induced decomposition due to the very low dose (0.001 ~ 1 A/cm^2) employed in those experiments.

7. Conclusion

This review demonstrated that the in situ nanobattery experiment inside TEM is a powerful paradigm for investigating the atomic and microstructural mechanisms of electrochemical energy conversion and material degradation in LIBs. With this approach, assisted by theory and modeling, we examined the
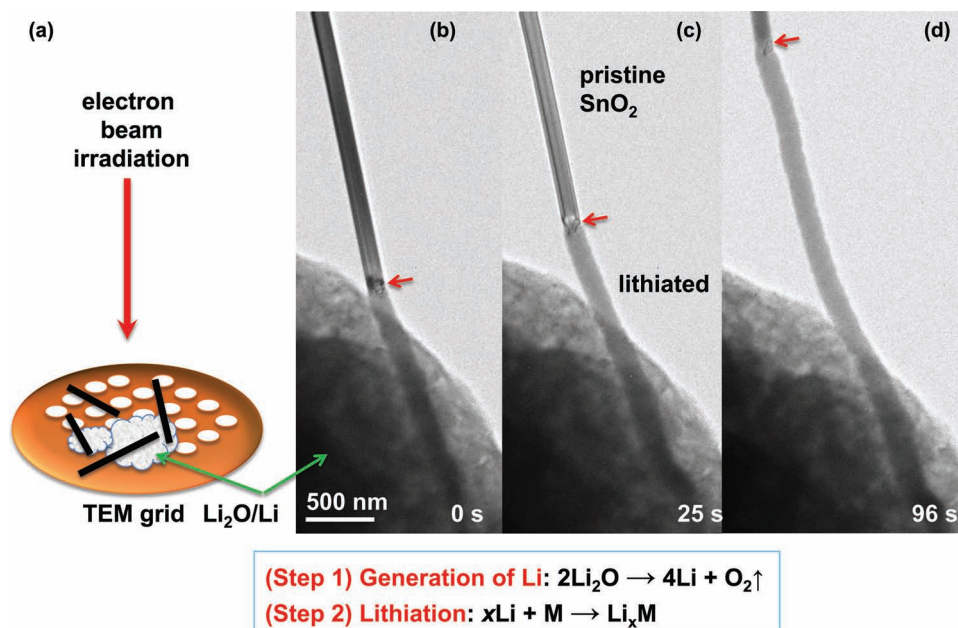
Figure 18. In situ chemical lithiation of SnO$_2$ nanowires using conventional TEM holder. (a) Schematic illustration of the experimental approach. Li metal is scratched onto the conventional 3-mm Cu grid, and nanomaterials of interest are dispersed onto the Li metal coated with native Li$_2$O. The Li$_2$O layer can be decomposed by the incident electron beam to in situ produce elemental Li, which then lithiate the adjacent nanomaterial by diffusion. In this method, no external bias or manipulation is needed, and the lithiation is easily controlled by the electron beam irradiation to generate Li. (b-d) Lithiation of a SnO$_2$ nanowire as a demonstration of the in situ chemical lithiation method. The nanowire showed the same microstructural changes as seen in the in situ electrochemical lithiation experiment conducted with a Nanofactory TEM-scanning tunneling microscopy (STM) holder.

electrochemical and mechanical responses of various anode materials, including Si, Ge, Al, SnO$_2$, ZnO, carbon nanotubes and graphene as well as important electrode coating materials such as Al$_2$O$_3$. While each electrode material shows certain unique behavior, we demonstrated that the size, geometry, and the coating layer are critical factors that govern the electrochemical reactions and mechanical degradation. Our studies advanced the fundamental understanding of the coupled mechano-electrochemical effects governed by these factors. The results are useful to the development of basic guidelines for the rational design of high-performance LIBs. The consistency of our in situ results with those obtained from ex situ experiments conducted in conventional electrochemical cells shows that the electrochemical-mechanical responses observed in situ are intrinsic to the electrode material. The high information throughput gained from the in situ studies in the form of video streams in addition to the quantitative and analytical information is extremely valuable. Such approach also opens up new opportunities for the study of cathode materials and more quantitative electrochemistry like galvanostatic cyclic voltammetry. In the former, subtle structural changes in the cathode materials could be revealed by high-resolution TEM in real time with its analytical capabilities; in the latter, a closer linkage between structural evolution and electrochemistry could be established. It is envisioned that the young but rapidly evolving field of in situ TEM electrochemistry will continue to turn up exciting new science regarding LIBs and will also extend its applications to broader branches of chemistry and materials science.

[1] M. Armand, J. M. Tarascon, *Nature* **2008**, *451*, 652–657.

[2] A. S. Arico, P. Bruce, B. Scrosati, J. M. Tarascon, W. Van Schalkwijk, *Nat. Mater.* **2005**, *4*, 366–377.

[3] J.-M. Tarascon, *Phil Trans. R. Soc. A* **2010**, *368*, 3227–3241.

[4] J.-S. Lee, S. T. Kim, R. Cao, N.-S. Choi, M. Liu, K. T. Lee, J. Cho, *Adv. Energy Mater.* **2011**, *1*, 34–50.

[5] J. F. M. Oudenhoven, L. Baggetto, P. H. L. Notten, *Adv. Energy Mater.* **2011**, *1*, 10–33.

[6] Y. M. Chiang, *Science* **2010**, *330*, 1485–1486.

[7] C. K. Chan, H. L. Peng, G. Liu, K. McIlwrath, X. F. Zhang, R. A. Huggins, Y. Cui, *Nat. Nanotechnol.* **2008**, *3*, 31–35.

[8] A. Magasinski, P. Dixon, B. Hertzberg, A. Kvit, J. Ayala, G. Yushin, *Nat. Mater.* **2010**, *9*, 353–358.

[9] L. Y. Beaulieu, K. W. Eberman, R. L. Turner, L. J. Krause, J. R. Dahn, *Electrochem. Solid-State Lett.* **2001**, *4*, A137–A140.

[10] M. Rosso, C. Brissot, A. Teyssot, M. Dolle, L. Sannier, J. M. Tarascon, R. Bouchetc, S. Lascaud, *Electrochim. Acta* **2006**, *51*, 5334–5340.

[11] D. Chen, S. Indris, M. Schulz, B. Gamer, R. Mönig, *J. Power Sources* **2011**, *196*, 6382–6387.

[12] F. Orsini, A. Du Pasquier, B. Beaudoin, J. M. Tarascon, M. Trentin, N. Langenhuizen, E. De Beer, P. Notten, *J. Power Sources* **1998**, *76*, 19–29.

[13] J. Y. Huang, L. Zhong, C. M. Wang, J. P. Sullivan, W. Xu, L. Q. Zhang, S. X. Mao, N. S. Hudak, X. H. Liu, A. Subramanian, H. Y. Fan, L. Qi, A. Kushima, J. Li, *Science* **2010**, *330*, 1515–1520.

[14] K. Yamamoto, Y. Iriyama, T. Asaka, T. Hirayama, H. Fujita, C. A. J. Fisher, K. Nonaka, Y. Sugita, Z. Ogumi, *Angew. Chem. Int. Ed.* **2010**, *49*, 4414–4417.

[15] X. H. Liu, J. Y. Huang, *Energy Environ. Sci.* **2011**, *4*, 3844–3860.

[16] M. N. Obrovac, L. Christensen, *Electrochem. Solid-State Lett.* **2004**, *7*, A93-A96.

[17] J. Li, J. R. Dahn, *J. Electrochem. Soc.* **2007**, *154*, A156-A161.

[18] T. D. Hatchard, J. R. Dahn, *J. Electrochem. Soc.* **2004**, *151*, A838-A842.

[19] R. Bhattacharyya, B. Key, H. L. Chen, A. S. Best, A. F. Hollenkamp, C. P. Grey, *Nat. Mater.* **2010**, *9*, 504–510.

[20] B. Key, R. Bhattacharyya, M. Morcrette, V. Seznec, J. M. Tarascon, C. P. Grey, *J. Am. Chem. Soc.* **2009**, *131*, 9239–9249.

[21] B. Key, M. Morcrette, J. M. Tarascon, C. P. Grey, *J. Am. Chem. Soc.* **2011**, *133*, 503–512.

[22] S. C. Chao, Y. C. Yen, Y. F. Song, Y. M. Chen, H. C. Wu, N. L. Wu, *Electrochem. Commun.* **2010**, *12*, 234–237.

[23] B. R. Long, M. K. Y. Chan, J. P. Greeley, A. A. Gewirth, *J. Phys. Chem. C* **2011**, *115*, 18916–18921.

[24] L. J. Hardwick, P. W. Ruch, M. Hahn, W. Scheifele, R. Kotz, P. Novak, *J. Phys. Chem. Solids* **2008**, *69*, 1232–1237.

[25] C. J. Wen, R. A. Huggins, *J. Solid State Chem.* **1981**, *37*, 271–278.

[26] A. N. Dey, *J. Electrochem. Soc.* **1971**, *118*, 1547–1549.

[27] P. Limthongkul, Y. I. Jang, N. J. Dudney, Y. M. Chiang, *Acta Mater.* **2003**, *51*, 1103–1113.

[28] P. Limthongkul, Y. I. Jang, N. J. Dudney, Y. M. Chiang, *J. Power Sources* **2003**, *119*, 604–609.

[29] W. J. Weydanz, M. Wohlfahrt-Mehrens, R. A. Huggins, *J. Power Sources* **1999**, *81–82*, 237–242.

[30] X. H. Liu, H. Zheng, L. Zhong, S. Huang, K. Karki, L. Q. Zhang, Y. Liu, A. Kushima, W. T. Liang, J. W. Wang, J.-H. Cho, E. Epstein, S. A. Dayeh, S. T. Picraux, T. Zhu, J. Li, J. P. Sullivan, J. Cumings, C. Wang, S. X. Mao, Z. Z. Ye, S. Zhang, J. Y. Huang, *Nano Lett.* **2011**, *11*, 3312–3318.

[31] X. H. Liu, L. Q. Zhang, L. Zhong, Y. Liu, H. Zheng, J. W. Wang, J.-H. Cho, S. A. Dayeh, S. T. Picraux, J. P. Sullivan, S. X. Mao, Z. Z. Ye, J. Y. Huang, *Nano Lett.* **2011**, *11*, 2251–2258.

[32] C. M. Wang, W. Xu, J. Liu, D. W. Choi, B. Arey, L. V. Saraf, J. G. Zhang, Z. G. Yang, S. Thevuthasan, D. R. Baer, N. Salmon, *J. Mater. Res.* **2010**, *25*, 1541–1547.

[33] N. de Jonge, F. M. Ross, *Nat. Nanotechnol.* **2011**, *6*, 695–704.

[34] X. H. Liu, L. Zhong, S. Huang, S. X. Mao, T. Zhu, J. Y. Huang, *ACS Nano* **2012**, *6*, 1522–1531.

[35] X. H. Liu, L. Zhong, L. Q. Zhang, A. Kushima, S. X. Mao, J. Li, Z. Z. Ye, J. P. Sullivan, J. Y. Huang, *Appl. Phys. Lett.* **2011**, *98*, 183107.

[36] X. H. Liu, S. Huang, S. T. Picraux, J. Li, T. Zhu, J. Y. Huang, *Nano Lett.* **2011**, *11*, 3991–3997.

[37] Y. Liu, N. S. Hudak, D. L. Huber, S. J. Limmer, J. P. Sullivan, J. Y. Huang, *Nano Lett.* **2011**, *11*, 4188–4194.

[38] Y. Liu, H. Zheng, X. H. Liu, S. Huang, T. Zhu, J. Wang, A. Kushima, N. S. Hudak, X. Huang, S. Zhang, S. X. Mao, X. Qian, J. Li, J. Y. Huang, *ACS Nano* **2011**, *5*, 7245–7253.

[39] X. H. Liu, J. W. Wang, Y. Liu, H. Zheng, A. Kushima, S. Huang, T. Zhu, S. X. Mao, J. Li, S. Zhang, W. Lu, J. M. Tour, J. Y. Huang, *Carbon* **2012**, DOI: 10.1016/j.carbon.2012.04.025.

[40] A. Kushima, X. H. Liu, G. Zhu, Z. L. Wang, J. Y. Huang, J. Li, *Nano Lett.* **2011**, *11*, 4535–4541.

[41] L. Q. Zhang, X. H. Liu, Y. Liu, S. Huang, T. Zhu, L. Gui, S. X. Mao, Z. Z. Ye, C. M. Wang, J. P. Sullivan, J. Y. Huang, *ACS Nano* **2011**, *5*, 4800–4809.

[42] L. Zhong, X. H. Liu, G. F. Wang, S. X. Mao, J. Y. Huang, *Phys. Rev. Lett.* **2011**, *106*, 248302.

[43] D. Larcher, S. Beattie, M. Morcrette, K. Edstroem, J. C. Jumas, J. M. Tarascon, *J. Mater. Chem.* **2007**, *17*, 3759–3772.

[44] B. A. Boukamp, G. C. Lesh, R. A. Huggins, *J. Electrochem. Soc.* **1981**, *128*, 725–729.

[45] M. N. Obrovac, L. J. Krause, *J. Electrochem. Soc.* **2007**, *154*, A103-A108.

[46] J. L. Goldman, B. R. Long, A. A. Gewirth, R. G. Nuzzo, *Adv. Funct. Mater.* **2011**, *21*, 2412–2422.

[47] H. J. Jung, M. Park, S. H. Han, H. Lim, S. K. Joo, *Solid State Commun.* **2003**, *125*, 387–390.

[48] S. Huang, T. Zhu, *J. Power Sources* **2011**, *196*, 3664–3668.

[49] S. H. Ng, J. Z. Wang, D. Wexler, K. Konstantinov, Z. P. Guo, H. K. Liu, *Angew. Chem. Int. Ed.* **2006**, *45*, 6896–6899.

[50] L. F. Cui, R. Ruffo, C. K. Chan, H. L. Peng, Y. Cui, *Nano Lett.* **2009**, *9*, 491–495.

[51] H. T. Nguyen, F. Yao, M. R. Zamfir, C. Biswas, K. P. So, Y. H. Lee, S. M. Kim, S. N. Cha, J. M. Kim, D. Pribat, *Adv. Energy Mater.* **2011**, *1*, 1154–1161.

[52] M. H. Park, M. G. Kim, J. Joo, K. Kim, J. Kim, S. Ahn, Y. Cui, J. Cho, *Nano Lett.* **2009**, *9*, 3844–3847.

[53] T. Ishihara, M. Nakasu, M. Yoshio, H. Nishiguchi, Y. Takita, *J. Power Sources* **2005**, *146*, 161–165.

[54] R. Huang, X. Fan, W. C. Shen, J. Zhu, *Appl. Phys. Lett.* **2009**, *95*, 133119.

[55] B. Hertzberg, A. Alexeev, G. Yushin, *J. Am. Chem. Soc.* **2010**, *132*, 8548–8549.

[56] O. M. Vovk, B. K. Na, B. W. Cho, J. K. Lee, *Korean J. Chem. Eng.* **2009**, *26*, 1034–1039.

[57] X. Zhao, C. M. Hayner, M. C. Kung, H. H. Kung, *Adv. Energy Mater.* **2011**, *1*, 1079–1084.

[58] K. Evanoff, A. Magasinski, J. Yang, G. Yushin, *Adv. Energy Mater.* **2011**, *1*, 495–498.

[59] M. H. Kong, D. J. Byun, J. K. Lee, in *Advanced Materials and Processing, Vol. 26–28* (Eds: Y. W. Chang, N. J. Kim, C. S. Lee), Trans Tech Publications, Switzerland **2007**, pp.333–336.

[60] M. H. Kong, J. H. Noh, D. J. Byun, J. K. Lee, *J. Electroceram.* **2009**, *23*, 376–381.

[61] L. Baggetto, E. J. M. Hensen, P. H. L. Notten, *Electrochim. Acta* **2010**, *55*, 7074–7079.

[62] L. Baggetto, P. H. L. Notten, *J. Electrochem. Soc.* **2009**, *156*, A169–A175.

[63] O. B. Chae, S. Park, J. H. Ku, J. H. Ryu, S. M. Oh, *Electrochim. Acta* **2010**, *55*, 2894–2900.

[64] C. K. Chan, X. F. Zhang, Y. Cui, *Nano Lett.* **2008**, *8*, 307–309.

[65] M. K. Y. Chan, B. R. Long, A. A. Gewirth, J. P. Greeley, *J. Phys. Chem. Lett.* **2011**, *2*, 3092–3095.

ADVANCED
ENERGY
MATERIALS
www.advenergymat.de

REVIEW

Materials
Views

www.MaterialsViews.com

[66] R. A. DiLeo, M. J. Ganter, R. P. Raffaelle, B. J. Landi, J. Mater. Res. 2010, 25, 1441–1446.

[67] Y. Kim, H. Hwang, K. Lawler, S. W. Martin, J. Cho, Electrochim. Acta 2008, 53, 5058–5064.

[68] B. Laforge, L. Levan-Jodin, R. Salot, A. Billard, J. Electrochem. Soc. 2008, 155, A181-A188.

[69] M.-H. Park, Y. Cho, K. Kim, J. Kim, M. Liu, J. Cho, Angew. Chem. Int. Ed. 2011, 50, 9647–9650.

[70] M. H. Seo, M. Park, K. T. Lee, K. Kim, J. Kim, J. Cho, Energy Environ. Sci. 2011, 4, 425–428.

[71] S. Yoon, C. M. Park, H. J. Sohn, Electrochem. Solid-State Lett. 2008, 11, A42-A45.

[72] J. Graetz, C. C. Ahn, R. Yazami, B. Fultz, J. Electrochem. Soc. 2004, 151, A698-A702.

[73] V. L. Chevrier, J. W. Zwanziger, J. R. Dahn, J. Alloys Compd. 2010, 496, 25–36.

[74] U. Kasavajjula, C. S. Wang, A. J. Appleby, J. Power Sources 2007, 163, 1003–1039.

[75] L. Baggetto, R. A. H. Niessen, F. Roozeboom, P. H. L. Notten, Adv. Funct. Mater. 2008, 18, 1057–1066.

[76] L. Baggetto, J. F. M. Oudenhoven, T. van Dongen, J. H. Klootwijk, M. Mulder, R. A. H. Niessen, M. H. J. M. de Croon, P. H. L. Notten, J. Power Sources 2009, 189, 402–410.

[77] M. R. St John, A. J. Furgala, A. F. Sammells, J. Electrochem. Soc. 1982, 129, 246–250.

[78] S. W. Lee, M. T. McDowell, J. W. Choi, Y. Cui, Nano Lett. 2011, 11, 3034–3039.

[79] H. Seidel, L. Csepregi, A. Heuberger, H. Baumgartel, J. Electrochem. Soc. 1990, 137, 3612–3626.

[80] B. Q. Wu, A. Kumar, S. Pamarthy, J. Appl. Phys. 2010, 108, 051101.

[81] E. I. Gladyshevskii, P. I. Kripyakevich, Soviet Physics, Crystallography 1960, 5, 549–551.

[82] Q. Johnson, G. S. Smith, D. Wood, Acta Crystallogr. 1965, 18, 131–132.

[83] X. H. Liu, J. W. Wang, H. Yang, S. Huang, F. Fan, X. Huang, Y. Liu, S. Krylyuk, J. Yoo, S. A. Dayeh, A. V. Davydov, S. X. Mao, S. T. Picraux, S. Zhang, J. Li , T. Zhu, J. Y. Huang, 2012, unpublished.

[84] T. Takamura, S. Ohara, M. Uehara, J. Suzuki, K. Sekine, J. Power Sources 2004, 129, 96–100.

[85] I. Ryu, J. W. Choi, Y. Cui, W. D. Nix, J. Mech. Phys. Solids 2011, 59, 1717–1730.

[86] T. K. Bhandakkar, H. J. Gao, Int. J. Solids Struct. 2010, 47, 1424–1434.

[87] T. K. Bhandakkar, H. Gao, Int. J. Solids Struct. 2011, 48, 2304–2309.

[88] M. J. Chon, V. A. Sethuraman, A. McCormick, V. Srinivasan, P. R. Guduru, Phys. Rev. Lett. 2011, 107, 045503.

[89] Y. P. Wu, E. Rahm, R. Holze, J. Power Sources 2003, 114, 228–236.

[90] B. J. Landi, M. J. Ganter, C. D. Cress, R. A. DiLeo, R. P. Raffaelle, Energy Environ. Sci. 2009, 2, 638–654.

[91] I. Lahiri, S. W. Oh, J. Y. Hwang, S. Cho, Y. K. Sun, R. Banerjee, W. Choi, ACS Nano 2010, 4, 3440–3446.

[92] B. Gao, A. Kleinhammes, X. P. Tang, C. Bower, L. Fleming, Y. Wu, O. Zhou, Chem. Phys. Lett. 1999, 307, 153–157.

[93] J. Y. Eom, H. S. Kwon, J. Liu, O. Zhou, Carbon 2004, 42, 2589–2596.

[94] S. Y. Chew, S. H. Ng, J. Z. Wang, P. Novak, F. Krumeich, S. L. Chou, J. Chen, H. K. Liu, Carbon 2009, 47, 2976–2983.

[95] B. Gao, C. Bower, J. D. Lorentzen, L. Fleming, A. Kleinhammes, X. P. Tang, L. E. McNeil, Y. Wu, O. Zhou, Chem. Phys. Lett. 2000, 327, 69–75.

[96] H. Shimoda, B. Gao, X. P. Tang, A. Kleinhammes, L. Fleming, Y. Wu, O. Zhou, Physica B 2002, 323, 133–134.

[97] S. W. Lee, N. Yabuuchi, B. M. Gallant, S. Chen, B. S. Kim, P. T. Hammond, Y. Shao-Horn, Nat. Nanotechnol. 2010, 5, 531–537.

[98] H. Shimoda, B. Gao, X. P. Tang, A. Kleinhammes, L. Fleming, Y. Wu, O. Zhou, Phys. Rev. Lett. 2001, 88, 015502.

[99] Y. A. Kim, M. Kojima, H. Muramatsu, S. Umemoto, T. Watanabe, K. Yoshida, K. Sato, T. Ikeda, T. Hayashi, M. Endo, M. Terrones, M. S. Dresselhaus, Small 2006, 2, 667–676.

[100] B. G. Demczyk, Y. M. Wang, J. Cumings, M. Hetman, W. Han, A. Zettl, R. O. Ritchie, Mater. Sci. Eng. A 2002, 334, 173–178.

[101] J. N. Coleman, U. Khan, W. J. Blau, Y. K. Gun'ko, Carbon 2006, 44, 1624–1652.

[102] C. Masarapu, V. Subramanian, H. W. Zhu, B. Q. Wei, Adv. Funct. Mater. 2009, 19, 1008–1014.

[103] V. G. Pol, M. M. Thackeray, Energy Environ. Sci. 2011, 4, 1904–1912.

[104] A. Boudaoud, P. Patricio, Y. Couder, M. Ben Amar, Nature 2000, 407, 718–720.

[105] A. Vaziri, L. Mahadevan, Proc. Natl. Acad. Sci. USA 2008, 105, 7913–7918.

[106] K. Persson, Y. Hinuma, Y. S. Meng, A. Van der Ven, G. Ceder, Phys. Rev. B 2010, 82, 125416.

[107] Y. Qi, S. J. Harris, J. Electrochem. Soc. 2010, 157, A741-A747.

[108] D. A. C. Brownson, D. K. Kampouris, C. E. Banks, J. Power Sources 2011, 196, 4873–4885.

[109] Y. Q. Sun, Q. O. Wu, G. Q. Shi, Energy Environ. Sci. 2011, 4, 1113–1132.

[110] H. Gleiter, MRS Bulletin 2009, 34, 456–464.

[111] F. Belliard, P. A. Connor, J. T. S. Irvine, Solid State Ionics 2000, 135, 163–167.

[112] P. A. Connor, F. Belliard, M. Behm, L. G. Tovar, J. T. S. Irvine, Ionics 2002, 8, 172–176.

[113] A. V. Vertkov, V. A. Evtikhin, I. E. Lyublinskii, A. A. Sychev, Sov. Mater. Sci. 1990, 26, 153–156.

[114] C. F. Old, J. Nucl. Mater. 1980, 92, 2–25.

[115] R. M. Boothby, J. Nucl. Mater. 1992, 186, 209–211.

[116] F. A. Shunk, W. R. Warke, Scripta Metall. 1974, 8, 519–526.

[117] J. O. Besenhard, M. Hess, P. Komenda, Solid State Ionics 1990, 40–1, 525–529.

[118] J. O. Besenhard, J. Yang, M. Winter, J. Power Sources 1997, 68, 87–90.

[119] X. F. Lei, J. X. Ma, Mater. Chem. Phys. 2009, 116, 383–387.

[120] M. Au, S. McWhorter, H. Ajo, T. Adams, Y. Zhao, J. Gibbs, J. Power Sources 2010, 195, 3333–3337.

[121] C. M. Park, J. H. Kim, H. Kim, H. J. Sohn, Chem. Soc. Rev. 2010, 39, 3115–3141.

[122] J. Morales, R. Trocoli, S. Franger, J. Santos-Pena, Electrochim. Acta 2010, 55, 3075–3082.

[123] K. E. Aifantis, S. A. Hackney, J. Power Sources 2011, 196, 2122–2127.

[124] C. Li, H. P. Zhang, L. J. Fu, H. Liu, Y. P. Wu, E. Ram, R. Holze, H. Q. Wu, Electrochim. Acta 2006, 51, 3872–3883.

[125] H. J. Kweon, J. Park, J. Seo, G. Kim, B. Jung, H. S. Lim, J. Power Sources 2004, 126, 156–162.

[126] A. M. Kannan, L. Rabenberg, A. Manthiram, Electrochem. Solid-State Lett. 2003, 6, A16–A18.

[127] A. Eftekhari, Solid State Ionics 2004, 167, 237–242.

[128] H. Miyashiro, Y. Kobayashi, S. Seki, Y. Mita, A. Usami, M. Nakayama, M. Wakihara, Chem. Mater. 2005, 17, 5603–5605.

[129] Y. J. Kim, T. J. Kim, J. W. Shin, B. Park, J. P. Cho, J. Electrochem. Soc. 2002, 149, A1337-A1341.

[130] S. W. Lee, K. S. Kim, H. S. Moon, H. J. Kim, B. W. Cho, W. I. Cho, J. B. Ju, J. W. Park, J. Power Sources 2004, 126, 150–155.

[131] Y. J. Kim, H. Kim, B. Kim, D. Ahn, J. G. Lee, T. J. Kim, D. Son, J. Cho, Y. W. Kim, B. Park, *Chem. Mater.* **2003**, *15*, 1505–1511.

[132] J. Cho, Y. J. Kim, T. J. Kim, B. Park, *J. Electrochem. Soc.* **2002**, *149*, A127–A132.

[133] J. Cho, T.-J. Kim, Y. J. Kim, B. Park, *Chem. Commun.* **2001**, 1074–1075.

[134] J. Cho, Y. J. Kim, T. J. Kim, B. Park, *Angew. Chem. Int. Ed.* **2001**, *40*, 3367–3369.

[135] Z. H. Chen, J. R. Dahn, *Electrochem. Solid-State Lett.* **2002**, *5*, A213–A216.

[136] Z. R. Zhang, H. S. Liu, Z. L. Gong, Y. Yang, *J. Power Sources* **2004**, *129*, 101–106.

[137] H. S. Liu, Z. R. Zhang, Z. L. Gong, Y. Yang, *Solid State Ionics* **2004**, *166*, 317–325.

[138] Z. X. Wang, L. J. Liu, L. Q. Chen, X. J. Huang, *Solid State Ionics* **2002**, *148*, 335–342.

[139] H. L. Zhao, G. Ling, W. H. Qiu, X. H. Zhang, *J. Power Sources* **2004**, *132*, 195–200.

[140] Y. Iriyama, H. Kurita, I. Yamada, T. Abe, Z. Ogumi, *J. Power Sources* **2004**, *137*, 111–116.

[141] Y. K. Sun, Y. S. Lee, M. Yoshio, K. Amine, *Electrochem. Solid-State Lett.* **2002**, *5*, A99–A102.

[142] J. Cho, C. S. Kim, S. I. Yoo, *Electrochem. Solid-State Lett.* **2000**, *3*, 362–365.

[143] I. D. Scott, Y. S. Jung, A. S. Cavanagh, Y. An, A. C. Dillon, S. M. George, S.-H. Lee, *Nano Lett.* **2011**, *11*, 414–418.

[144] Y. S. Jung, A. S. Cavanagh, L. A. Riley, S. H. Kang, A. C. Dillon, M. D. Groner, S. M. George, S. H. Lee, *Adv. Mater.* **2010**, *22*, 2172–2176.

[145] Y. S. Jung, A. S. Cavanagh, A. C. Dillon, M. D. Groner, S. M. George, S.-H. Lee, *J. Electrochem. Soc.* **2010**, *157*, A75-A81.

[146] Y. He, X. Yu, Y. Wang, H. Li, X. Huang, *Adv. Mater.* **2011**, *23*, 4938–4941.

[147] A. M. Glass, K. Nassau, *J. Appl. Phys.* **1980**, *51*, 3756–3761.

[148] X. Xiao, P. Lu, D. Ahn, *Adv. Mater.* **2011**, *23*, 3911–3915.

[149] P. Vajda, F. Beuneu, *Phys. Rev. B* **1996**, *53*, 5335–5340.

[150] G. Krexner, M. Prem, F. Beuneu, P. Vajda, *Phys. Rev. Lett.* **2003**, *91*, 135502.